Submitted to the 29th International Conference on High-Energy Physics ICHEP98,
Vancouver, Canada, July 1998

Elastic Electroproduction of ρ Mesons for $1 < Q^2 < 60 \ \mathrm{GeV}^2$ at HERA

H1 Collaboration

Abstract

The cross section for the elastic electroproduction of ρ mesons is measured at HERA with the H1 detector, for the photon virtuality in the range $1 < Q^2 < 60 \ \mathrm{GeV}^2$ and for the hadronic centre of mass energy in the range $30 < W < 140$ GeV, using 1995 shifted vertex and 1996 data sets. The shape of the ρ mass distribution is studied as a function of Q^2. The full set of ρ spin density matrix elements is measured, and signifiant evidence is found for a helicity flip component. Measurements are presented of the dependence of the cross section on Q^2, W and t (the four-momentum transfer squared to the proton). The W dependence of the $\gamma^* p$ cross section becomes stronger as Q^2 rises.

Abstract: 564
Parallel session: 5
Plenary session: 7

1 Introduction

This paper presents a measurement of elastic ρ meson electroproduction:

$$e + p \to e + \rho + p, \quad \rho \to \pi^+ + \pi^-, \tag{1}$$

in the Q^2 range from 1 to 60 GeV^2 (Q^2 is the negative of the intermediate photon four-momentum squared) and the W range from 30 to 140 GeV (W is the hadronic centre of mass energy).

The data were obtained with the H1 detector in two running periods of the HERA collider, operated with 820 GeV protons and 27.5 GeV positrons. The lower Q^2 data set ($1 < Q^2 < 5$ GeV^2) was obtained from a special run in 1995, with the ep interaction vertex shifted by 70 cm in the outgoing proton beam direction, corresponding to an integrated luminosity of 125 nb^{-1} [1]. A larger sample ($2.5 < Q^2 < 60$ GeV^2) was obtained in 1996, under normal running conditions, and corresponds to a luminosity of 3.87 pb^{-1} [2].

The present measurement provides for the first time at high energy detailed information in the region from $Q^2 \sim 1$ GeV^2 to $Q^2 \sim 8$ GeV^2, and it increases the precision of the H1 measurement of ρ electroproduction with $Q^2 > 8$ GeV^2, which was first performed using data collected in 1994 [3].

The H1 detector, the event selection and the measurement of kinematic variables are introduced in section 2. The acceptances, efficiencies and backgrounds are discussed in section 3. The shape of the (π, π) candidate mass distribution and its evolution with Q^2 are studied in section 4. Section 5 is devoted to the study of the decay angular distributions and of the ρ meson spin density matrix elements, as a function of several kinematic variables. Finally, section 6 presents the t distribution and the measurement of the $\gamma^* p \to \rho p$ cross section, as a function of Q^2 and W.

2 H1 Detector, Event Selection and Kinematics

Events corresponding to reaction (1) are selected by requiring the detection in the H1 apparatus [4] of the scattered positron and of a pair of pions with opposite charges originating from a common vertex. The absence of additional activity in the detector is also required, since the scattered proton generally escapes undetected into the beam pipe.

In the following, the z axis is taken along the beam direction, the $+z$ or "forward" direction being that of the outgoing proton beam. The x axis points towards the centre of the HERA ring and the y axis is directed upwards.

2.1 The H1 Detector

The scattered positron is detected in the SPACAL, a lead – scintillating fibre spaghetti calorimeter situated in the backward region of the H1 detector, at 152 cm from the nominal interaction point. The calorimeter is divided into an electromagnetic and a hadronic part. The electromagnetic part of the SPACAL, which covers the angular range $153° < \theta < 177.5°$ (defined with respect to the nominal interaction point), is segmented in cells of 4×4 cm^2 transverse size. The hadronic section is used to veto hadrons faking a positron candidate. In front of the SPACAL, a set of drift chambers, the BDC, allows the reconstruction of positron track segments, providing a resolution in the transverse position of 0.5 mm.

The pion candidates are detected and their momentum is measured mainly in the central tracking detector. The major components of this detector are two 2 m long cylindrical drift chambers, the CJC "jet" chambers, of inner and outer radii respectively 203 and 451 mm, and 530 and 844 mm, with wires parallel to the beam direction. In the forward region, they are supplemented by a set of planar drift chambers perpendicular to the beam direction. The measurement of charged particle transverse momenta is performed in a magnetic field of 1.2 T, uniform over the full tracker volume, generated by a superconducting solenoidal magnet situated outside the calorimeter and the tracking detector. For charged particles emitted from the nominal vertex with polar angles $20^\circ < \theta < 160^\circ$, the resolution on the measurement of the transverse momentum is $\Delta p_t/p_t \simeq 1.\ 10^{-2}\ p_t$ (GeV). Drift chambers with wires perpendicular to the beam direction, sitting inside the inner jet chamber and between the two jet chambers, provide a measurement of z coordinates with a precision of 350 $\mu\mathrm{m}$.

The (x, y, z) position of the interaction vertex is reconstructed for each event by a global fit of all measured charged particle trajectories. For each positron fill in the accelerator, a fit is performed of the dependence of the x and y positions of the vertices as a function of z. This provides a measurement of the corresponding beam direction, which varies slightly from fill to fill.

The absence of additional activity in the H1 detector is checked using several components. The liquid argon (LAr) calorimeter, surrounding the tracking detector, covers the polar angular range $4^\circ \le \theta \le 153^\circ$ with full azimuthal acceptance. The muon spectrometer FMD, designed to identify and measure the momentum of forward muons, contains six active layers, each made of a pair of planes of drift cells, covering the angles $3^\circ \le \theta \le 17^\circ$. The three layers situated between the main calorimeter and the toroidal magnet of the FMD can be reached by secondary particles arising from the interaction in the beam collimators and the beam pipe walls of small angle primary particles. Similarly, secondary particles or the scattered proton at high $|t|$ can reach a set of scintillators, the proton remnant tagger PRT, placed 24 m downstream of the interaction point and covering the angles $0.06^\circ \le \theta \le 0.17^\circ$.

2.2 Trigger and Event Selection

The trigger and selection criteria for the events used in this analysis are summarised in table 1. Events are selected only from runs with stable and well monitored HERA beams, and for which all relevant parts of the detector were efficiently functioning.

For the 1995 shifted vertex run, the trigger used to select the data was based on the detection in the electromagnetic section of the SPACAL calorimeter of a cluster of energy larger than 12 GeV. For the 1996 data, the energy threshold was increased to 15 GeV and, in order to reduce the event rate, the centre of gravity of the cluster was required to lie outside the "box" region $-16 < x < 8$ cm and $-8 < y < 16$ cm. Additional trigger settings were used to check the efficiency of this trigger.

For the off-line data selection, the positron candidate must be associated with a well identified electromagnetic cluster in the SPACAL, with energy larger than 17 GeV and correlated with a track segment in the BDC. The transverse position of the BDC track has to be more than 8.7 cm from the beams for the 1995 data sample, and must lie within the trigger box for the 1996 data.

Two, and only two, opposite charge pion candidates are required, with polar angles of emission $20^\circ < \theta < 160^\circ$ and transverse momentum with respect to the beam direction $p_t > 0.1$ GeV, in order to ensure efficient detection and reconstruction in the central tracker. The reconstructed interaction vertex has to lie within 30 cm of the nominal interaction point.

Rejection of ρ meson events with proton dissociation and of other backgrounds is achieved by requiring the absence in the LAr calorimeter of any cluster with energy larger than 0.5 GeV that is not associated with the pion candidates, and by requiring that there be no more than one hit pair recorded in the FMD and no signal in the PRT. Given the limiting angle of 20° for pion candidates, this results in requiring no activity in a range in pseudorapidity $1.5 < \eta < 1.75$ [1].

The cuts $1 < Q^2 < 60$ GeV^2 and $30 < W < 140$ GeV, which define the kinematic domain under study, are related to the positron and track requirements. The $|t| < 0.5$ GeV^2 cut has a double purpose: it suppresses events with flatter t distributions than for elatic ρ production, in particular ρ production with proton dissociation; it also suppresses events with additional non-detected particles, which deteriorate the transverse momentum balance of the event used to compute t (see eq. 8). A further cut $E - p_z > 45$ GeV, where $E - p_z$ is calculated from the positron and the two pion candidates, is designed to minimise radiative corrections.

The selected domain for $m_{\pi\pi}$, the invariant mass of the two pion candidates, is restricted to $0.6 < m_{\pi\pi} < 1.1$ GeV, which covers the ρ meson mass peak and avoids the large distance regions where the ρ resonance shape is not well controlled (see section 4) and where other resonances are present. In order to minimise ϕ meson contamination, the invariant mass of the pion candidates is computed under the assumption that they are kaons, and the cut $m_{KK} > 1.040$ GeV is applied on the corresponding m_{KK} mass.

2.3 Kinematic Variables

The reconstruction method for the kinematic variables is chosen in order to achieve the best precision in the measurement.

The Q^2 variable is computed from $E_\circ$, the incident electron beam energy, and the angles θ_e and θ_ρ of the positron and of the ρ meson candidates [5]:

$$Q^2 = 4E_\circ^2 \frac{\sin\theta_\rho\,(1+\cos\theta_e)}{\sin\theta_\rho + \sin\theta_e - \sin(\theta_e+\theta_\rho)}. \tag{2}$$

The positron emission angles are determined using the reconstructed vertex position and the track segment in the BDC. The momentum of the ρ meson is reconstructed as the sum of those of the two pion candidates:

$$\vec{p}_\rho = \vec{p}_{\pi^+} + \vec{p}_{\pi^-}. \tag{3}$$

The inelasticity y is defined as

$$y = \frac{p\cdot q}{p\cdot k}, \tag{4}$$

[1] The pseudorapidity η of an object detected with polar angle θ with respect to the nominal vertex position is defined as $\eta = -\log\ \tan(\theta/2)$.

where p, k and q are, respectively, the four-momenta of the incident proton, of the incident positron and of the exchanged photon. For this analysis, y is computed using the energy E_ρ and the longitudinal momentum p_{z_ρ} of the ρ meson candidate [6]:

$$y = \frac{E_\rho - p_{z_\rho}}{2\ E_\mathrm{o}}. \tag{5}$$

The hadronic mass W is computed using the relation

$$W^2 = ys - Q^2, \tag{6}$$

where s is the ep invariant mass.

The t variable is the square of the four-momentum transfer to the proton. To very good precision, its absolute value is equal to the square of the transverse momentum of the outgoing proton, which is computed, under the assumption that the selected event corresponds to reaction (1), as the sum of the transverse momenta $\vec{p}_{t_\rho}$ of the ρ meson candidate and $\vec{p}_{t_e}$ of the scattered positron:

$$t \simeq -|\vec{p}_{t_\rho} + \vec{p}_{t_e}|^2. \tag{7}$$

The value of t is thus distorted if the event is not due to reaction (1), in particular if additional particles have been emitted but not detected. For computing t, the positron energy E_e is estimated from the ρ candidate measurement and the positron beam energy using the relation

$$E_e = \frac{2E_\mathrm{o} - E_\rho + p_{z_\rho}}{1 - \cos\theta_e}. \tag{8}$$

This relation assumes reaction (1) and the absence of QED radiation.

Finally, the variable $E - p_z$ is computed as the sum of the differences between the energies and the longitudinal momenta of the positron and pion candidates, where the positron energy measured in the SPACAL calorimeter is used.

3 Smeared Acceptances, Efficiencies and Backgrounds

3.1 Smeared Acceptances and Efficiencies. The DIFFVM Monte-Carlo

Acceptances, efficiencies and smearing effects are computed using mainly the DIFFVM Monte-Carlo simulation [7], a program based on the vector meson dominance model.

The DIFFVM parameters are adjusted and the generated distributions are weighted following the measurements presented below for the dependence of the cross section on Q^2, W, t and, under the s-channel helicity conservation prescription, in two variables which govern the ρ meson angular decay distributions: R, the ratio of the longitudinal to transverse photon cross sections, and the $\cos\delta$ parameter, which measures the interference between the longitudinal and transverse amplitudes. The dependence of the cross section on these variables is parameterised as a function of Q^2, as measured in the present data.

For this simulation, the detector geometry and its response to generated particles are simulated in detail, under the conditions corresponding respectively to the 1995 and 1996 runs. The same reconstruction procedures as for real events are applied. As an illustration of the good quality of the simulation, fig. 1 presents a comparison of the distributions of several variables for the data and the Monte-Carlo.

In the kinematic domain defined in table 1, the major acceptance effect is the Q^2 dependence, which is of purely geometrical origin and is due to the restriction of the accepted domain in the SPACAL imposed for the trigger. The cuts on the polar angle and on the minimum transverse momentum of the pion candidates induce W-dependent acceptance corrections which are sensitive to the correct simulation of the ρ meson angular distributions. The acceptance effects in Q^2 and in W are correlated, which explains the Q^2 dependence of the selected W domains defined in table 1. The cut on $E - p_z$ induces very small corrections.

For each of the measurements presented below, a systematic error is computed, for which negative and positive contributions are combined separately in the form of a quadratic sum. The systematic errors due to the smeared acceptances are computed by varying by ± 0.5 mrad the positron polar angle, and by varying the dependences in Q^2, W, t, R and $\cos\delta$ in the Monte-Carlo simulation over the range allowed by the present measurement.

In addition to the effects studied with the DIFFVM simulation, the trigger efficiency is studied using several independent triggers. Regions of the SPACAL for which the trigger efficiency is less than 80 % are discarded from the measurement. In the remaining regions, the trigger efficiency varies between 94 and 100 %, and the data are corrected as a function of Q^2. Losses of elastic events due to noise in the LAr, FMD and PRT detectors are computed directly from the data, using information from random read-outs of the detector, not correlated with a physics trigger.

3.2 Backgrounds

The main backgrounds to ρ meson elastic production are due to elastic production of ω and ϕ mesons and to diffractive ρ production with proton dissociation.

3.2.1 Elastic Production of ω and ϕ Mesons

The elastic production rate of ω mesons:

$$e + p \rightarrow e + \omega + p \tag{9}$$

is about 11 % of that of ρ mesons, following the quark additive model. Two decay channels:

$$\omega \rightarrow \pi^+ + \pi^- + \pi^o \qquad (\mathrm{BR} = 88.8\%) \tag{10}$$

$$\omega \rightarrow \pi^+ + \pi^- \qquad (\mathrm{BR} = 2.2\%) \tag{11}$$

contribute events which may be selected in the present sample. The first channel contribution is efficiently reduced by requiring the absence in the LAr calorimeter of clusters with energy larger than 0.5 GeV, by the mass selection cut and by the cut on the variable t. However, events from the second channel are selected within the present sample.

The production rate of ϕ mesons:

$$e + p \rightarrow e + \phi + p \tag{12}$$

is a Q^2-dependent fraction of the ρ production rate, which amounts to about 15 % for the present data [8, 1]. The following decay channels may lead to a background in the selected sample:

$$\phi \to K^+ + K^- \qquad (\mathrm{BR} = 49.1\%) \tag{13}$$

$$\phi \to \rho + \pi \qquad (\mathrm{BR} = 12.9\%) \tag{14}$$

$$\phi \to \pi^+ + \pi^- + \pi^o \qquad (\mathrm{BR} = 2.7\%). \tag{15}$$

The first contribution is mostly eliminated by the m_{KK} and the $m_{\pi\pi}$ mass selection cuts, and the other two are significantly reduced by the LAr, t and mass selection cuts.

Using the DIFFVM Monte-Carlo, the remaining contributions of ω and ϕ elastic production in the selected sample are estimated to be 1.4 and 1.9 %, respectively, in the invariant mass range 0.6 $< m_{\pi\pi} <$ 1.1 GeV. To study the shape of the mass distribution (see sect. 4), the $m_{\pi\pi}$ range used is 0.5 $< m_{\pi\pi} <$ 1.1 GeV, where the contributions of ω and ϕ elastic production are estimated to be 4.7 and 2.3 %.

3.2.2 Diffractive Production of ρ Mesons with Proton Dissociation

An important background to ρ elastic production is due to the diffractive production of ρ mesons with proton dissociation

$$e + p \to e + \rho + Y, \tag{16}$$

when the baryonic system Y is of relatively low mass M_Y and its decay products are not detected in the PRT, the FMD or the forward regions of the LAr and the tracking detector.

The contamination from proton dissociation is estimated using the DIFFVM Monte-Carlo. The distribution of M_Y is generated according to the law [9]

$$\frac{\mathrm{d}\sigma}{\mathrm{d}M_Y^2} \propto \frac{1}{M_Y^2}. \tag{17}$$

For $M_Y <$ 1.9 GeV, the events are weighted to describe the details of resonance production, and decays are simulated following the Particle Data Group (PDG) tables [10]. For larger masses, the system decays to a quark and a diquark, which fragment according to the JETSET algorithm [11]. The t distribution of proton dissociation events is modelled by an exponentially falling distribution with a slope parameter $b = 2.5$ GeV^{-2} (cf. the measurements in [8] and [12]). The DIFFVM Monte-Carlo is also used to compute the probability that an elastic ρ event with $|t| <$ 0.5 GeV^2 gives a signal in the forward detectors (in practice, the PRT).

The proton dissociation background in the selected sample is estimated from the numbers of events with or without a signal in the PRT or the FMD, and satisfying all other criteria of table 1, and from the probabilities for elastic and proton dissociation events to give a signal in these detectors, estimated using the Monte-Carlo models. This procedure avoids making hypotheses concerning the relative production rates for elastic and inelastic events. The proton dissociation background in the present sample amounts to $11 \pm 5\%$. The uncertainty on this number is estimated by varying by ± 0.3 the exponent of the M_Y distribution in eq. 17, and by computing this correction using only the PRT or only the FMD.

3.2.3 Other Backgrounds

Other backgrounds are negligibly small. The background due to the $\pi^+\pi^-\pi^o\pi^o$ decay mode of the $\rho'(1450)$ meson is estimated to be $1 \pm 1\%$, in particular due to the cuts on the variable t and on the energy deposits in the LAr calorimeter. The study of the mass distributions presented in section 4 also indicates that events with photon dissociation into vector mesons other than ρ, ω and ϕ do not contribute more than 1 %, when skewing effects are taken into account [2]. The background of photoproduction events with a hadron faking the electron candidate in the SPACAL is extremely small, because of the high E_e cut.

4 Mass Distributions

Figs. 2 and 3 present the distributions of $m_{\pi\pi}$, the invariant $\pi^+\pi^-$ mass, for the events passing the selection cuts of table 1, in five domains in Q^2. The ω and ϕ backgrounds (see section 3.2.1) are subtracted according to their mass distribution obtained from the DIFFVM Monte-Carlo, and uniformly in Q^2.

The mass distributions are skewed compared to a Breit-Wigner shape: an enhancement is observed in the low mass region and a suppression at the high mass side. This effect has been attributed to an interference between the resonant and non–resonant production of two pions [13]. In order to extract the contribution of the resonant part of the cross section, two different procedures are used.

Following the phenomenological parameterisation of Ross and Stodolsky [14], the $m_{\pi\pi}$ distribution is described as:

$$\frac{\mathrm{d}N(m_{\pi\pi})}{\mathrm{d}m_{\pi\pi}} = f_\rho \; BW_\rho(m_{\pi\pi}) \; (\frac{m_\rho}{m_{\pi\pi}})^n + f_{bg}, \tag{18}$$

where f_ρ is a normalisation constant and

$$BW_\rho(m_{\pi\pi}) = \frac{m_{\pi\pi} \; m_\rho \; \Gamma(m_{\pi\pi})}{(m_\rho^2 - m_{\pi\pi}^2)^2 + m_\rho^2 \; \Gamma^2(m_{\pi\pi})} \tag{19}$$

is a relativistic Breit-Wigner function with momentum dependent width [16]

$$\Gamma(m_{\pi\pi}) = \Gamma_\rho \; (\frac{q^*}{q_0^*})^3 \; \frac{2}{1 + (q^*/q_0^*)^2}. \tag{20}$$

Here, Γ_ρ is the ρ resonance width, q^* is the pion momentum in the $(\pi^+\pi^-)$ rest frame and q_0^* is this momentum when $m_{\pi\pi} = m_\rho$. The factor $(m_\rho/m_{\pi\pi})^n$ in eq. 18 accounts for the skewing of the shape of the ρ signal. The background term f_{bg} is parameterised using a phase space distribution, including a two pion threshold and an exponential fall off:

$$f_{bg} = \alpha_1 \; (m_{\pi\pi} - 2m_\pi)^{\alpha_2} \; e^{-\alpha_3 m_{\pi\pi}}, \tag{21}$$

[2] In the analysis of the 1994 data [3], with $Q^2 > 8$ GeV^2 and smaller statistics than for the present analysis, no significant evidence was found for the presence of skewing at large Q^2, and the distortion of the $m_{\pi\pi}$ distribution was attributed to a contribution of $11 \pm 6\%$ non-resonant background, which was subtracted from the cross section. In the present analysis, the distortion of the mass spectrum is attributed to skewing effects, see section 4.

where m_π is the pion mass and α_1, α_2 and α_3 are constants.

With eq. 18, the mass distribution for the selected events with $2.5 < Q^2 < 60$ GeV^2 is fit over the range $0.5 < m_{\pi\pi} < 1.1$ GeV, with the parameters f_ρ, m_ρ, Γ_ρ, n, α_1, α_2 and α_3 left free. The resonance mass is found to be 0.766 ± 0.004 GeV and the width 0.155 ± 0.006 GeV, in agreement with the the PDG values of 0.770 and 0.151 GeV [10]. The fit value of the skewing parameter is $n = 1.40 \pm 0.18$ and the background contribution corresponds to 1 ± 1 % of the number of events in the peak. The fit is of good quality: $\chi^2/\mathrm{ndf} = 20.3/17$.

For the five Q^2 domains presented in fig. 2, fits to the form of eq. 18 are thus performed with the mass and the width of the ρ meson fixed to the PDG values, in order to reduce statistical uncertainties, and assuming the absence of non-resonant background ($f_{bg} = 0$). This leaves two free parameters: the overall normalisation and the skewing parameter n. The fit values of n are presented in fig. 4, the χ^2/ndf values being good in all bins.

The data are also analysed using the parameterisation proposed by Söding [15], in which the skewing of the mass spectrum is explained by the interference of a resonant $\rho \to \pi^+\pi^-$ amplitude and a p-wave $\pi\pi$ Drell type background term:

$$\frac{\mathrm{d}N(m_{\pi\pi})}{\mathrm{d}m_{\pi\pi}} = f_\rho\, BW_\rho(m_{\pi\pi}) + f_I\, I(m_{\pi\pi}) + f_{bg}, \tag{22}$$

$$I(m_{\pi\pi}) = \frac{m_\rho^2 - m_{\pi\pi}^2}{(m_\rho^2 - m_{\pi\pi}^2)^2 + m_\rho^2\, \Gamma^2(m_{\pi\pi})}, \tag{23}$$

where f_I is a constant fixing the relative normalisation of the interference contribution. In view of the uncertainties in the phase between the resonant and the non-resonant amplitudes, no constraint is imposed on the relative contributions of the background and interference terms.

The Söding parameterisation also describes the data well in the range $0.5 < m_{\pi\pi} < 1.1$ GeV, with values for the resonance mass and width in agreement with the PDG values and non-resonant background compatible with 0. For the five selected bins, the width and the mass of the ρ meson are thus fixed and no background is assumed. Fits to the normalisation and the skewing parameter f_I/f_ρ are again good, and the results are presented in fig. 3.

Fig. 4 shows the fit values of the skewing parameters as a function of Q^2, together with the results of previous measurements. In this figure, the inner error bars on the 1996 data points are purely statistical and the full error bars include both statistical and systematic errors added in quadrature. The systematic errors are computed as described in section 3.1. The skewing of the mass distribution is observed to decrease with Q^2. No significant W or t dependence of the skewing is observed within the data.

5 Helicity Study

5.1 Angular Decay Distribution

The study of the angular distributions of the two pions coming from the decay of the ρ meson gives information on the helicity state of the ρ meson. The decay angles are defined in three reference frames [17]: the helicity system, the Gottfried-Jackson system, and the Adlair system. In the helicity system, used for the present measurement, the ρ direction in the $\gamma^* p$ centre of mass system (cms) is taken as the quantization axis. Three angles are defined as follows: the polar (θ) and azimuthal (φ) angles of the positive pion from the ρ meson decay in the $\pi^+\pi^-$ cms, and the angle ϕ between the ρ production plane and the electron scattering plane, in the $\gamma^* p$ cms.

Following the formalism used in [18], the decay angular distribution W($\cos\theta$, φ, ϕ) is expressed as a function of 15 matrix elements in the form:

$$
\begin{aligned}
W(\cos\theta,\varphi,\phi) = \frac{3}{4\pi} \ & \Big\{ \ \frac{1}{2}(1-r^{04}_{00}) + \frac{1}{2}(3\,r^{04}_{00}-1)\ \cos^2\theta \\
& -\sqrt{2}\ \mathrm{Re}\, r^{04}_{10}\ \sin 2\theta\cos\varphi - r^{04}_{1-1}\ \sin^2\theta\cos 2\varphi \\
& -\varepsilon\ \cos 2\phi \Big(r^1_{11}\ \sin^2\theta + r^1_{00}\ \cos^2\theta - \sqrt{2}\ \mathrm{Re}\, r^1_{10}\ \sin 2\theta\cos\varphi \\
& \qquad - r^1_{1-1}\ \sin^2\theta\cos 2\varphi \Big) \\
& -\varepsilon\ \sin 2\phi \Big(\sqrt{2}\ \mathrm{Im}\, r^2_{10}\ \sin 2\theta\sin\varphi + \mathrm{Im}\, r^2_{1-1}\ \sin^2\theta\sin 2\varphi \Big) \\
& +\sqrt{2\varepsilon\,(1+\varepsilon)}\ \cos\phi\ \Big(\text{-}r^5_{11}\ \sin^2\theta + r^5_{00}\ \cos^2\theta \\
& \qquad -\sqrt{2}\ \mathrm{Re}\, r^5_{10}\ \sin 2\theta\cos\varphi - r^5_{1-1}\ \sin^2\theta\cos 2\varphi \Big) \\
& +\sqrt{2\varepsilon\,(1+\varepsilon)}\ \sin\phi\ \Big(\sqrt{2}\ \mathrm{Im}\, r^6_{10}\ \sin 2\theta\sin\varphi \\
& \qquad +\mathrm{Im}\, r^6_{1-1}\ \sin^2\theta\sin 2\varphi \Big) \Big\}.
\end{aligned} \tag{24}
$$

where ε is the polarisation parameter of the incident photon beam (at HERA, $\langle\varepsilon\rangle$ = 0.99). The 15 matrix elements are related to various combinations of the helicity amplitudes $T_{\lambda_\rho\lambda_{N'},\lambda_\gamma\lambda_N}$, where λ_ρ and λ_γ are, respectively, the helicities of the ρ meson and of the photon, λ_N and $\lambda_{N'}$ being respectively the helicities of the incoming and outgoing proton [3].

The 15 matrix elements, determined from the average of the projections of the decay angular distribution (eq. 24) onto orthogonal functions ("moment method", see [18], Appendix C), are presented in table 2. The statistical and systematic errors are given separately. The results are also presented in figs. 5−7 for three bins in Q^2, three bins in W and three bins in t. Here, and in the rest of section 5, the systematic errors are computed as described in section 3.1. The data sample is not corrected for the presence of ρ production events with proton dissociation, for the small presence of backgrounds of ω and ϕ production and for radiative effects.

The measurement can be interpreted in the light of additional approximations.

- Natural parity exchange
  For the case of natural parity exchange (NPE), the quantum numbers exchanged in the t-channel have natural parity (P = (-1)^J) and

$$T_{-\lambda_\rho\lambda_{N'},-\lambda_\gamma\lambda_N} = (-1)^{\lambda_\rho-\lambda_\gamma}\ T_{\lambda_\rho\lambda_{N'},\lambda_\gamma\lambda_N}. \tag{25}$$

  The use of the NPE approximation in the s-channel heliciry frame in this paper is relevant since the $|t|$ values are small ($|t| < 0.5$ GeV^2).

[3] As noted in [19], only the components $\lambda_\gamma = \pm 1$ contribute to the normalisation factor N_T in Appendix A of [18].

- s–channel helicity conservation
  For the case of s-channel helicity conservation (SCHC), the helicity of the virtual photon is retained by the ρ meson:

$$T_{\lambda_\rho \lambda_{N'}, \lambda_\gamma \lambda_N} = T_{\lambda_\rho \lambda_{N'}, \lambda_\gamma \lambda_N} \; \delta_{\lambda_\rho \lambda_\gamma} \; \delta_{\lambda_{N'} \lambda_N}. \tag{26}$$

  Single and double helicity flip amplitudes are then zero (the nucleon helicities being omitted):

$$T_{\lambda_\rho \lambda_\gamma} = T_{01} = T_{10} = T_{0-1} = T_{-10} = 0, \tag{27}$$

$$T_{-11} = T_{1-1} = 0. \tag{28}$$

In the SCHC approximation, all matrix elements are zero except for five of them [18]:

$$r^{04}_{00}, \quad r^{1}_{1-1} \; = \; - \,\mathrm{Im}\, r^{2}_{1-1}, \quad \mathrm{Re}\, r^{5}_{10} \; = \; - \,\mathrm{Im}\, r^{6}_{10}. \tag{29}$$

Table 3 gives the expressions for the 15 matrix elements as a function of the helicity amplitudes in the NPE and the SCHC approximations. The measurements of the matrix elements are in good agreement with the NPE and SCHC predictions, except for the r^5_{00} matrix element (see table 2).

The results presented in table 2 are discussed in section 5.2 in the SCHC approximation, and in section 5.3 the violation of the SCHC approximation is studied. For these analyses, the decay angular distribution W($\cos\theta$, φ, ϕ) is integrated over 2 of the 3 angles, in order to extract information from the shapes of the one-dimensional distributions.

5.2 The Longitudinal and Transverse Cross Sections

5.2.1 The r^{04}_{00} Matrix Element

The r^{04}_{00} matrix element can be computed from the $\cos\theta$ distribution, as shown from the angular distribution (eq. 24) after integration over the φ and ϕ angles:

$$W(\cos\theta) \propto 1 - r^{04}_{00} + (3\, r^{04}_{00} - 1) \; \cos^2\theta. \tag{30}$$

In fig. 8, the $\cos\theta$ distribution is presented in six bins in Q^2, and a fit of eq. 30 is superimposed. The results of the measurement of r^{04}_{00} are presented in fig. 9 in six bins in Q^2, three bins in W and three bins in t.

In the s-channel helicity conservation approximation, the matrix element r^{04}_{00} is related to R, the cross section ratio for ρ production by longitudinal and transverse virtual photons:

$$R = \frac{\sigma_L}{\sigma_T} = \frac{1}{\varepsilon} \frac{r^{04}_{00}}{1 - r^{04}_{00}}. \tag{31}$$

As observed in table 2 and discussed in section 5.3, the SCHC violating amplitudes are small compared to the helicity conserving amplitudes T_{00} and T_{11}. At first order, SCHC is thus used to estimate R. The results are presented in fig. 10, as a function of Q^2, together with other measurements performed with the same approximation.

5.2.2 Longitudinal–Transverse Interference

In the NPE and SCHC approximations, the decay angular distribution W($\cos\theta$, φ, ϕ) reduces to a function of two variables: $\cos\theta$ and ψ, the difference of the angles ϕ and φ:

$$W(\cos\theta,\psi) = \frac{3}{8\pi}\,\frac{1}{1+\varepsilon\,R}\,\Big\{\sin^2\theta\,(1+\varepsilon\,\cos 2\psi) + 2\,\varepsilon\,R\,\cos^2\theta - \sqrt{2\varepsilon\,(1+\varepsilon)\,R}\,\cos\delta\sin 2\theta\cos\psi\Big\}\,, \qquad (32)$$

where δ is the phase between the transverse T_{11} and the longitudinal T_{00} amplitudes:

$$T_{00}\,T_{11}^\dagger = |T_{00}|\,|T_{11}|\,e^{-i\delta} \qquad (33)$$

and

$$\cos\delta = \frac{1+\varepsilon\,R}{\sqrt{R/2}}\,(\mathrm{Re}\,r^5_{10} - \mathrm{Im}\,r^6_{10}\,)\,. \qquad (34)$$

A scatter plot of the $\cos\theta$ and ψ variables is presented in fig. 11. A fit of eq. 32 to the data gives:

$$\cos\delta = 0.925 \pm 0.022\,^{+0.011}_{-0.022}. \qquad (35)$$

This number is in agreement within errors with the value of $\cos\delta$ computed from eq. 34, using the measurements of Re r^5_{10} and Im r^6_{10} given in table 2. Fig. 12 presents the values of $\cos\delta$ obtained when dividing the data into three bins in Q^2, three bins in W and three bins in t.

A measurement of the r^1_{1-1} matrix element can be obtained by integrating the W($\cos\theta$, ψ) distribution over $\cos\theta$:

$$W(\psi) = \frac{1}{2\pi}\,(1+2\,\varepsilon\,r^1_{1-1}\,\cos 2\psi). \qquad (36)$$

The ψ distributions are shown for five Q^2 bins in fig. 13. Fits of eq. 36 to the data, shown superimposed on fig. 13, provide measurements of the r^1_{1-1} matrix element. The results are presented in fig. 14 in five bins in Q^2, three bins in W and three bins in t.

5.3 Helicity Conservation and Helicity Flip Amplitudes

In table 2 and figs. 5–7, the r^5_{00} matrix element is observed to be significantly different from the null value expected in the case of SCHC. This matrix element can also be extracted from the measurement of the angle ϕ, as shown from the integration of the decay angular distribution (eq. 24) over $\cos\theta$ and φ:

$$W(\phi) \propto 1 - \varepsilon\,\cos 2\phi\,(\frac{1}{2}r^1_{11} + r^1_{00}) + \sqrt{2\varepsilon(1+\varepsilon)}\cos\phi\,(\frac{1}{2}r^5_{11} + r^5_{00}). \qquad (37)$$

The corresponding distributions are presented in fig. 15 for six bins in Q^2 and in fig. 16 for four bins in t. The combinations of the matrix elements $(\frac{1}{2}r^1_{11} + r^1_{00})$ and $(\frac{1}{2}r^5_{11} + r^5_{00})$, extracted in six Q^2 bins, three W bins and four t bins are presented in fig. 17. As the matrix elements r^1_{11} and r^5_{11} are measured to be compatible with zero (see table 2), the values obtained for the two combinations of matrix elements can be reduced to the matrix elements r^1_{00} and r^5_{00} respectively.

The non-zero values obtained for the r^5_{00} matrix element are in agreement with a recent model from Ivanov and Kirschner based on perturbative QCD, where two hard gluons are exchanged in the interaction [20]. This model predicts a violation of SCHC at high Q^2, the largest helicity-flip amplitude being T_{01}, with:

$$1 > \alpha = \frac{T_{11}}{T_{00}} > \beta = \frac{T_{01}}{T_{00}} > \delta = \frac{T_{10}}{T_{00}} > \eta = \frac{T_{1-1}}{T_{00}} \tag{38}$$

for the HERA kinematical domain. In the NPE and $T_{10} = T_{-11} = 0$ approximations, the matrix elements are expressed as a function of the helicity amplitudes in table 3 (second column).

One observes in table 3 that among the matrix elements which vanish for SCHC, r^5_{00} deviates most substantially from zero, as expected in the model of [20] from eq. 38 ($r^5_{00} \propto \beta$). Furthermore, a dependence of the helicity-flip amplitude T_{01} in t is predicted in [20]:

$$T_{01} \propto \frac{\sqrt{|t|}}{m_\rho} T_{11} \tag{39}$$

and this trend is suggested in the data (see fig. 17). The predicted values for the 15 matrix elements [20] are in good agreement, within experimental errors, with the present measurements.

Using the expression for the r^5_{00} matrix element given in the second column of table 3, and supposing purely imaginary amplitudes [20], the ratio of the helicity flip to non flip amplitudes can be estimated:

$$\frac{|T_{01}|}{\sqrt{|T_{11}|^2 + |T_{00}|^2}} \simeq \frac{|T_{01}|}{|T_{11}|\sqrt{1+R}} \simeq r^5_{00} \sqrt{\frac{1+R}{2R}} \tag{40}$$

$$\simeq 8.0 \pm 3.0\%. \tag{41}$$

Another way to study the violation of the SCHC approximation under the NPE hypothesis is to compare the values of the r^1_{1-1} matrix element obtained respectively from the $\cos\theta$ distributions and from the ψ distributions. In the SCHC and NPE approximations, r^1_{1-1} is related to r^{04}_{00} by the relation:

$$r^1_{1-1} = \frac{1}{2}\,(1 - r^{04}_{00}). \tag{42}$$

Using this relation and the values of the r^{04}_{00} matrix element extracted from the $\cos\theta$ distributions (presented in fig. 9), one obtains measurements of the matrix element r^1_{1-1} in five bins in Q^2, three bins in W and three bins in t. These values are compared in table 4 to those obtained from fits of the ψ distribution (presented in fig. 14). One observes that the two sets of numbers differ at the 2 σ level at high Q^2. This confirms a slight violation of SCHC (in the NPE approximation).

Finally, the integration of eq. 24 over $\cos\theta$ and ϕ allows the extraction of the r^{04}_{1-1} matrix element:

$$W(\varphi) \propto 1 - 2\, r^{04}_{1-1} \cos 2\varphi. \tag{43}$$

The result of a fit to this equation for r^{04}_{1-1} is given in fig. 18 for six bins in Q^2, confirming that this matrix element is consistent with 0. This is in agreement with the SCHC predictions (see table 3) and the Ivanov-Kirschner model, for which the matrix element r^{04}_{1-1} is proportional to the small helicity flip amplitude T_{10} and the double helicity flip amplitude T_{1-1} [20].

6 Cross Sections

6.1 t Distribution

The t distributions of the selected events with $|t| < 0.5$ GeV^2 are presented in fig. 19 for five bins in Q^2. To study the t dependence of elastic ρ production, these distributions are fitted as the sum of three exponentials, corresponding respectively to the elastic component with free slope parameter b, to the background of diffractive ρ events with proton dissociation, which amounts to $11 \pm 5\%$ of the elastic signal (see section 3.2.2), with a fixed slope $b_{pd} = 2.5 \pm 1.0$ GeV^{-2}, and to the non-resonant background amounting to $1 \pm 1\%$ of the signal, with slope $b_{nr} = 0.3 \pm 0.1$ GeV^{-2}.

The fitted b slopes for elastic events are presented as a function of Q^2 in fig. 20. The systematic errors are computed by varying the parameters of the Monte-Carlo simulation used for the smeared acceptance corrections (see section 3.1), by varying the amounts of backgrounds and their slopes within the quoted errors, and by varying the binning and the limits of the fits.

The present measurement confirms the decrease of b with increasing Q^2, reflecting the decrease of the transverse size of the $q\bar{q}$ system emerging from the photon. It is observed in fig. 20 that at low Q^2 ($Q^2 \lesssim 3$ GeV^2) measurements at HERA lie systematically above the fixed targets results of CHIO [21], NMC [22] and E665 [23]. This may be explained by the shrinkage of the diffractive peak as W increases. However, within the W range of the present experiment, and given the experimental errors, no significant information can be extracted on a possible shrinkage of the t distribution at higher Q^2.

6.2 Q^2 Dependence of the Cross Section

The $\gamma^* p$ cross section for ρ elastic production is extracted from the ep cross section using the relation:

$$\frac{\mathrm{d}^2\sigma(ep \to e\rho p)}{\mathrm{d}y \; \mathrm{d}Q^2} = \Gamma \; \sigma(\gamma^* p \to \rho p) = \Gamma \; \sigma_T(\gamma^* p \to \rho p) \; (1 + \varepsilon R), \tag{44}$$

where Γ is the flux of virtual photons, given for small values of y by:

$$\Gamma \simeq \frac{\alpha \, (1 - y + y^2/2)}{\pi \; y \; Q^2}, \tag{45}$$

where α is the fine structure constant.

The $\gamma^* p$ cross section is presented as a function of Q^2 in fig. 21. It is computed for a Breit-Wigner distribution of the resonance mass, after a Q^2 dependent correction for the skewing effects described in section 4, within five width values Γ_ρ (see eq. 20) around the ρ pole mass:

$$2 \, m_\pi \leq m_{\pi\pi} \leq m_\rho \; + 5 \; \Gamma_\rho. \tag{46}$$

The cross section measured in each bin is corrected following the W dependence measured in section 6.3, so that all cross sections are quoted for a common value of $W = 75$ GeV.

The backgrounds of ρ diffractive production with proton dissociation, of ω and ϕ elastic production, and the non-resonant background are subtracted uniformly as a function of Q^2. The uncertainties on these backgrounds are included in the systematic errors.

The Q^2-dependent losses induced by the $|t| < 0.5$ GeV^2 cut are corrected for on a bin by bin basis, according to the measured b slopes (see section 6.1). The effects of the smeared acceptances and efficiencies and their errors are estimated as described in section 3.1. The errors on the extrapolations of the cross sections to the common value of $W = 75$ GeV and to the quoted Q^2 values are estimated by varying the W and the Q^2 dependences of the cross section in the limits of the present measurements. Radiative corrections are estimated using the HERACLES program [24]. They are found to be very small when the kinematic variables are computed as described in section 2.3 and for the value chosen for the $E - p_z$ cut. A correction of 1.00 ± 0.04 is thus applied, where the 4 % error accounts for the uncertainties in the Q^2 and W dependences of the cross section when computing the radiative corrections, for higher order processes and for detector effects not taken into account with the HERACLES program. The systematic errors also include an uncertainty of 2 % on the luminosity measurement, and the uncertainties due to limited Monte Carlo statistics.

In fig 21, the inner error bars on the data points are purely statistical and the full error bars include both statistical and systematic errors added in quadrature.

The Q^2 dependence of the ρ meson elastic electroproduction cross section is parameterised in the form:

$$\sigma(\gamma^* p) \propto \frac{1}{(Q^2 + m_\rho^2)^n}, \tag{47}$$

with

$$n = 2.24 \pm 0.09. \tag{48}$$

The result of a fit of eq. 47 is shown as a full line in fig. 21. For this fit, the the statistical and the non-correlated systematic errors are used. The quality of the fit for the full Q^2 range $1 \leq Q^2 \leq 35$ GeV^2 is good: χ^2/ndf = 13.3 / 20. In the present analysis, a common normalisation is used for the 1995 and 1996 data sets, which agree within one standard deviation.

6.3 W Dependence of the Cross Section

The $\gamma^* p$ cross section for ρ elastic production is presented as a function of W for six Q^2 values in fig. 22. The extrapolation of the measured cross sections to the chosen Q^2 values are performed using the Q^2 dependence given by eqs. 47 and 48. Corrections and systematic errors are estimated as for the Q^2 dependence study in section 6.2.

A stronger W dependence of the cross section is suggested when Q^2 increases. In order to quantify this effect, the W dependence of the cross section is fitted for each Q^2 bin to a form inspired by Regge theory:

$$\sigma(\gamma^* p) \propto W^{4(\langle \alpha(t) \rangle - 1)}. \tag{49}$$

The results of the fits are presented in fig. 22. In this figure, the inner error bars on the data points are purely statistical and the full error bars include both statistical and systematic errors added in quadrature. For the fit of eq. 49 to the data, only the statistical and the non-correlated systematic errors are used, the χ^2/ndf values being raisonable for each Q^2 value.

In a Regge context, $\alpha(t)$ is interpreted as describing the exchange trajectory, with:

$$\alpha(t) = \alpha(0) + \alpha' \, t, \tag{50}$$

$$\alpha(0) = 1 + \epsilon. \tag{51}$$

To extract from the fit results the ϵ parameter, $\langle t \rangle = 1/b$ is taken from the measured values (see section 6.1) and, in the absence of a measurement of the Q^2 dependence of the shrinkage of the t distribution, the value $\alpha' = 0.25$ GeV^{-2} measured in hadron−hadron interactions [25] is assumed. The values obtained for the ϵ parameter as a function of Q^2 are shown in fig. 23. The inner error bars come from the statistical and non-correlated systematic uncertainties on the cross section measurements, the outer error bars include the systematic variation of the ϵ parameter when supposing $\alpha' = 0$, added in quadrature. An indication for an increase of ϵ with Q^2 is observed: at high Q^2, ϵ is measured to be higher than the 0.08 value observed in hadron−hadron experiments [25], but with large errors.

7 Summary and Conclusions

The elastic electroproduction of ρ mesons has been studied at HERA with the H1 detector, for $1 < Q^2 < 60$ GeV^2 and $30 < W < 140$ GeV. The data sets, corresponding respectively to 125 nb^{-1} for $1 < Q^2 < 5$ GeV^2 and 3.87 pb^{-1} for $2.5 < Q^2 < 60$ GeV^2, were taken in 1995 with the ep interaction vertex shifted by 70 cm in the outgoing proton beam direction, and in 1996 under normal running conditions.

The shape of the $(\pi\pi)$ mass distribution has been studied as a function of Q^2, and indicates significant but decreasing skewing effects, up to $Q^2 \gtrsim 10$ GeV^2.

The full set of 15 elements characterising the ρ spin density matrix has been measured as a function of Q^2, W and t, using the decay angular distributions defined in the helicity frame. Under the assumption of natural parity exchange, s-channel helicity conservation is found to be a good approximation, except for a small but significant deviation from zero of the r^5_{00} element. For $Q^2 \gtrsim 2$ GeV^2, the longitudinal $\gamma^* p$ cross section becomes larger than the transverse cross section, and the ratio R reaches values of $R \simeq 3$ for $Q^2 \simeq 20$ GeV^2. The phase δ between the longitudinal and transverse amplitudes is measured as $\cos\delta = 0.925 \pm 0.022$. The dominant helicity flip amplitude $T_{\lambda_\rho=0,\lambda_\gamma=1}$ is found to be 8 ± 3 % of the non-flip amplitudes, slightly increasing with $|t|$. The prediction of a model of ρ meson electroproduction of Ivanov and Kirschner is in good agreement with the measurement of the matrix elements.

The t distribution for ρ electroproduction has been studied, and the exponential b slope is found to decrease with Q^2.

The $\gamma^* p \to \rho p$ cross section has been measured over the domain $1 < Q^2 < 35$ GeV^2. The Q^2 dependence is well described by the function $1/(Q^2 \; + m^2_\rho)^n$, with $n = 2.24 \pm 0.09$.

The W dependence of the $\gamma^* p \to \rho p$ cross section has been measured for six Q^2 values. The $\gamma^* p$ cross section is found to rise with W, this dependence becoming stronger as Q^2 rises. At high Q^2, the ϵ parameter is measured to be higher than the 0.08 value observed in hadron−hadron experiments [25], but with large errors.

Acknowledgements

We are grateful to the HERA machine group whose outstanding efforts made this experiment possible. We appreciate the immense effort of the engineers and technicians who constructed and maintained the detector. We thank the funding agencies for their financial support of the experiment. We wish to thank the DESY directorate for the support and hospitality extended to the non-DESY members of the collaboration. We thank further D. Yu. Ivanov for useful discussions.

References

[1] The corresponding results were presented in:
H1 Coll., *Elastic Electroproduction of ρ and ϕ Mesons for $1 < Q^2 < 5$ GeV^2 at HERA*, paper 381, subm. to the Int. Europhys. Conf. on HEP, Jerusalem, Israel, 1997.

[2] B. Clerbaux, PhD Thesis, Université Libre de Bruxelles, in preparation.

[3] S. Aid et al., H1 Coll., *Nucl. Phys.* **468** (1996) 3.

[4] A detailed description of the H1 detector can be found in:
I. Abt et al., H1 Coll., *Nucl. Instr. Meth.* **386** (1997) 310; *Nucl. Instr. Meth.* **386** (1997) 348.

[5] S. Bentvelsen, J. Engelen and P. Kooijman, *Reconstruction of (x, Q^2) and extraction of structure functions in neutral current scattering at HERA,* in: Proc. of the Workshop on Physics at HERA, ed. W. Buchmüller and G. Ingelman, Hamburg 1992, Vol. 1, p. 23;
K.C. Hoeger, *Measurement of x, y, Q^2 in Neutral Current Events,* ibid., p. 43.

[6] F. Jacquet, A. Blondel, DESY 79-048(1979)377.

[7] *DIFFVM program,* see: B. List, *Diploma Thesis*, Techn. Univ. Berlin, unpubl. (1993).

[8] C. Adloff et al, H1 Coll., *Zeit. Phys.* **C75** (1997) 607.

[9] K. Goulianos, *Phys. Rep.* **101** (1983) 169

[10] R.M. Barnett et al., *Review of Particle Properties, Phys. Rev.* **D54** (1996) 1.

[11] T. Sjöstrand, *PYTHIA 5.7 and JETSET 7.4. Physics and Manual,* preprint CERN-TH.7112/93 (1993) (revised February 1994).

[12] X. Janssen, Mémoire de Licence, Université Libre de Bruxelles, 1998, unpubl.

[13] S.D. Drell, *Phys. Rev. Lett.* **5** (1960) 278.

[14] R. Ross and V. Stodolsky, *Phys. Rev.* **149** (1966) 1173.

[15] P. Söding, *Phys. Lett.* **B19** (1966) 702.

[16] T.J. Jackson, *Nuovo Cim.* **34** (1964) 1644.

[17] T.H. Bauer et al., *Rev. Mod. Phys.* **50** (1978) 261.

[18] K. Shilling and G. Wolff, *Nucl. Phys.* **B61** (1973) 381.

[19] P. Joos et al., *Nucl. Phys.* **B113** (1976) 53.

[20] D. Yu. Ivanov and R. Kirschner, “Polarization in diffractive electroproduction of light vector mesons”, hep-ph/9807324.

[21] W.D. Shambroom et al., CHIO Coll., *Phys. Rev.* **D26** (1982) 1.

[22] P. Amaudruz et al., NMC Coll., *Zeit. Phys.* **C54** (1992) 239;
M. Arneodo et al., NMC Coll., *Nucl. Phys.* **B429** (1994) 503.

[23] M. R. Adams et al., *Zeit. Phys.* **C74** (1997) 237

[24] H. Spiesberger, *HERACLES 4.4,* unpublished program manual (1993);
A. Kwiatkowski, H. Spiesberger and H.-J. Möhring, *An event generator for ep interactions at HERA including radiative processes,* in: Proc. of the Workshop on Physics at HERA, ed. W. Buchmüller and G. Ingelman, Hamburg 1992, Vol. 3, p. 1294.

[25] A. Donnachie, P.V. Landshoff, *Phys. Lett.* **B296** (1992) 227.

Trigger	cluster in SPACAL with energy > 15 GeV in selected domain
Positron	cluster in electromagnetic SPACAL with energy > 17 GeV distance between cluster c.o.g. and BDC track < 3 cm transverse width of cluster < 3.2 cm energy in hadronic SPACAL < 0.2 GeV
Pion candidates	2 tracks with opposite signs $20° < \theta < 160°$ particle transverse momenta $p_t > 0.1$ GeV vertex reconstructed within 30 cm of nominal position in z
Additional activity	no cluster in LAr with energy > 0.5 GeV at most 1 hit pair in FMD no hit in PRT
Mass selection	$0.6 < m_{\pi\pi} < 1.1$ GeV $m_{KK} > 1.040$ GeV
Kinematic domain 1995 data 1996 data	 $1.0 < Q^2 < 5$ GeV^2, $40 < W < 140$ GeV $2.5 < Q^2 < 4$ GeV^2, $30 < W < 100$ GeV $4.0 < Q^2 < 6$ GeV^2, $30 < W < 120$ GeV $6.0 < Q^2 < 14$ GeV^2, $40 < W < 140$ GeV $14.0 < Q^2 < 60$ GeV^2, $50 < W < 140$ GeV
Other cuts	$\|t\| < 0.5$ GeV^2 $E - p_z > 45$ GeV

Table 1: Summary of trigger conditions and event selection criteria.

Element	measurement		
r^{04}_{00}	0.674	$\pm$ 0.018	$^{+0.051}_{-0.036}$
Re r^{04}_{10}	0.011	$\pm$ 0.012	$^{+0.007}_{-0.001}$
r^{04}_{1-1}	-0.010	$\pm$ 0.013	$^{+0.004}_{-0.003}$
r^{1}_{00}	-0.058	$\pm$ 0.048	$^{+0.013}_{-0.011}$
r^{1}_{11}	0.002	$\pm$ 0.034	$^{+0.006}_{-0.006}$
Re r^{1}_{10}	-0.018	$\pm$ 0.016	$^{+0.010}_{-0.014}$
r^{1}_{1-1}	0.122	$\pm$ 0.018	$^{+0.004}_{-0.005}$
Im r^{2}_{10}	0.023	$\pm$ 0.016	$^{+0.010}_{-0.009}$
Im r^{2}_{1-1}	-0.119	$\pm$ 0.018	$^{+0.010}_{-0.005}$
r^{5}_{00}	0.093	$\pm$ 0.024	$^{+0.019}_{-0.010}$
r^{5}_{11}	0.008	$\pm$ 0.017	$^{+0.008}_{-0.012}$
Re r^{5}_{10}	0.146	$\pm$ 0.008	$^{+0.006}_{-0.006}$
r^{5}_{1-1}	-0.004	$\pm$ 0.009	$^{+0.001}_{-0.003}$
Im r^{6}_{10}	-0.140	$\pm$ 0.008	$^{+0.002}_{-0.004}$
r^{6}_{1-1}	0.002	$\pm$ 0.009	$^{+0.003}_{-0.000}$

Table 2: Spin density matrix elements for the elastic electroproduction of ρ mesons, measured using moments of the projections of the angular decay distribution (24) onto orthogonal functions of the ρ meson production and decay angles.

element	NPE and $T_{1-1} = T_{10} = 0$	NPE and SCHC
r^{04}_{00}	$\frac{1}{1+\epsilon R}\left(\frac{\|T_{01}\|^2}{\|T_{11}\|^2+\|T_{01}\|^2} + \epsilon R\right)$	$\frac{\epsilon R}{1+\epsilon R}$
$\mathrm{Re}\, r^{04}_{10}$	$\frac{1}{1+\epsilon R}\ \frac{1}{2(\|T_{11}\|^2+\|T_{01}\|^2)}\ \mathrm{Re}\,(T_{11}T^{\dagger}_{01})$	0
r^{04}_{1-1}	0	0
r^{1}_{00}	$\frac{-1}{1+\epsilon R}\ \frac{\|T_{01}\|^2}{\|T_{11}\|^2+\|T_{01}\|^2}$	0
r^{1}_{11}	0	0
$\mathrm{Re}\, r^{1}_{10}$	$-\mathrm{Re}\, r^{04}_{10}$	0
r^{1}_{1-1}	$\frac{1}{2}\ \frac{1}{1+\epsilon R}\ \frac{\|T_{11}\|^2}{\|T_{11}\|^2+\|T_{01}\|^2}$	$\frac{1}{2}\frac{1}{1+\epsilon R}$
$\mathrm{Im}\, r^{2}_{10}$	$\mathrm{Re}\, r^{04}_{10}$	0
$\mathrm{Im}\, r^{2}_{1-1}$	$-r^{1}_{1-1}$	$-r^{1}_{1-1}$
r^{5}_{00}	$\sqrt{2}\frac{\sqrt{R}}{1+\epsilon R}\ \frac{1}{\|T_{00}\|\sqrt{\|T_{11}\|^2+\|T_{01}\|^2}}\ \mathrm{Re}\,(T_{00}T^{\dagger}_{01})$	0
r^{5}_{11}	0	0
$\mathrm{Re}\, r^{5}_{10}$	$\frac{\sqrt{2}}{4}\ \frac{\sqrt{R}}{1+\epsilon R}\ \frac{1}{\|T_{00}\|\sqrt{\|T_{11}\|^2+\|T_{01}\|^2}}\ \mathrm{Re}\,(T_{11}T^{\dagger}_{00})$	$\frac{\sqrt{2}}{4}\ \frac{\sqrt{R}}{1+\epsilon R}\ \frac{1}{\|T_{11}\|\|T_{00}\|}\mathrm{Re}\,(T_{11}T^{\dagger}_{00})$
r^{5}_{1-1}	0	0
$\mathrm{Im}\, r^{6}_{10}$	$-\mathrm{Re}\, r^{5}_{10}$	$-\mathrm{Re}\, r^{5}_{10}$
r^{6}_{1-1}	0	0

Table 3: Second column: the spin density matrix elements for the elastic electroproduction of ρ mesons, expressed as a function of the helicity amplitudes $T_{\lambda_\rho\,\lambda_\gamma}$, under the NPE hypothesis and neglecting the helicity flip amplitude T_{10} and the double-flip amplitude T_{1-1}. Third column: the spin density matrix elements under the SCHC and NPE approximations (i.e. neglecting in addition the T_{01} helicity flip amplitude)

Q^2 (GeV^2)	W (GeV)	t (GeV^2)	r^1_{1-1} from (42)	r^1_{1-1} from ψ distrib.
2.5-4	30-100	0-0.5	$0.169 \pm 0.020\ ^{+0.013}_{-0.012}$	$0.156 \pm 0.025\ ^{+0.006}_{-0.010}$
4-6	30-120	0-0.5	$0.156 \pm 0.020\ ^{+0.002}_{-0.006}$	$0.090 \pm 0.035\ ^{+0.008}_{-0.019}$
6-9	30-140	0-0.5	$0.137 \pm 0.022\ ^{+0.002}_{-0.011}$	$0.098 \pm 0.042\ ^{+0.012}_{-0.009}$
9-14	30-140	0-0.5	$0.115 \pm 0.026\ ^{+0.013}_{-0.007}$	$0.021 \pm 0.056\ ^{+0.022}_{-0.019}$
14-60	30-140	0-0.5	$0.139 \pm 0.035\ ^{+0.017}_{-0.009}$	$0.019 \pm 0.074\ ^{+0.010}_{-0.041}$
2.5-60	40-60	0-0.5	$0.162 \pm 0.017\ ^{+0.013}_{-0.015}$	$0.204 \pm 0.030\ ^{+0.008}_{-0.010}$
2.5-60	60-80	0-0.5	$0.140 \pm 0.018\ ^{+0.013}_{-0.014}$	$0.093 \pm 0.033\ ^{+0.025}_{-0.025}$
2.5-60	80-100	0-0.5	$0.164 \pm 0.020\ ^{+0.007}_{-0.008}$	$0.076 \pm 0.040\ ^{+0.040}_{-0.036}$
2.5-60	30-140	0-0.1	$0.159 \pm 0.013\ ^{+0.012}_{-0.014}$	$0.104 \pm 0.024\ ^{+0.017}_{-0.018}$
2.5-60	30-140	0.1-0.2	$0.165 \pm 0.017\ ^{+0.014}_{-0.025}$	$0.120 \pm 0.032\ ^{+0.012}_{-0.026}$
2.5-60	30-140	0.2-0.5	$0.176 \pm 0.017\ ^{+0.016}_{-0.017}$	$0.128 \pm 0.031\ ^{+0.005}_{-0.006}$

Table 4: Matrix element r^1_{1-1} in 5 bins in Q^2, 3 bins in W and 3 bins in t. In column 4, the value of r^1_{1-1} is obtained from the r^{04}_{00} matrix element using relation 42. In column 5, the value of r^1_{1-1} is extracted from the ψ distributions.

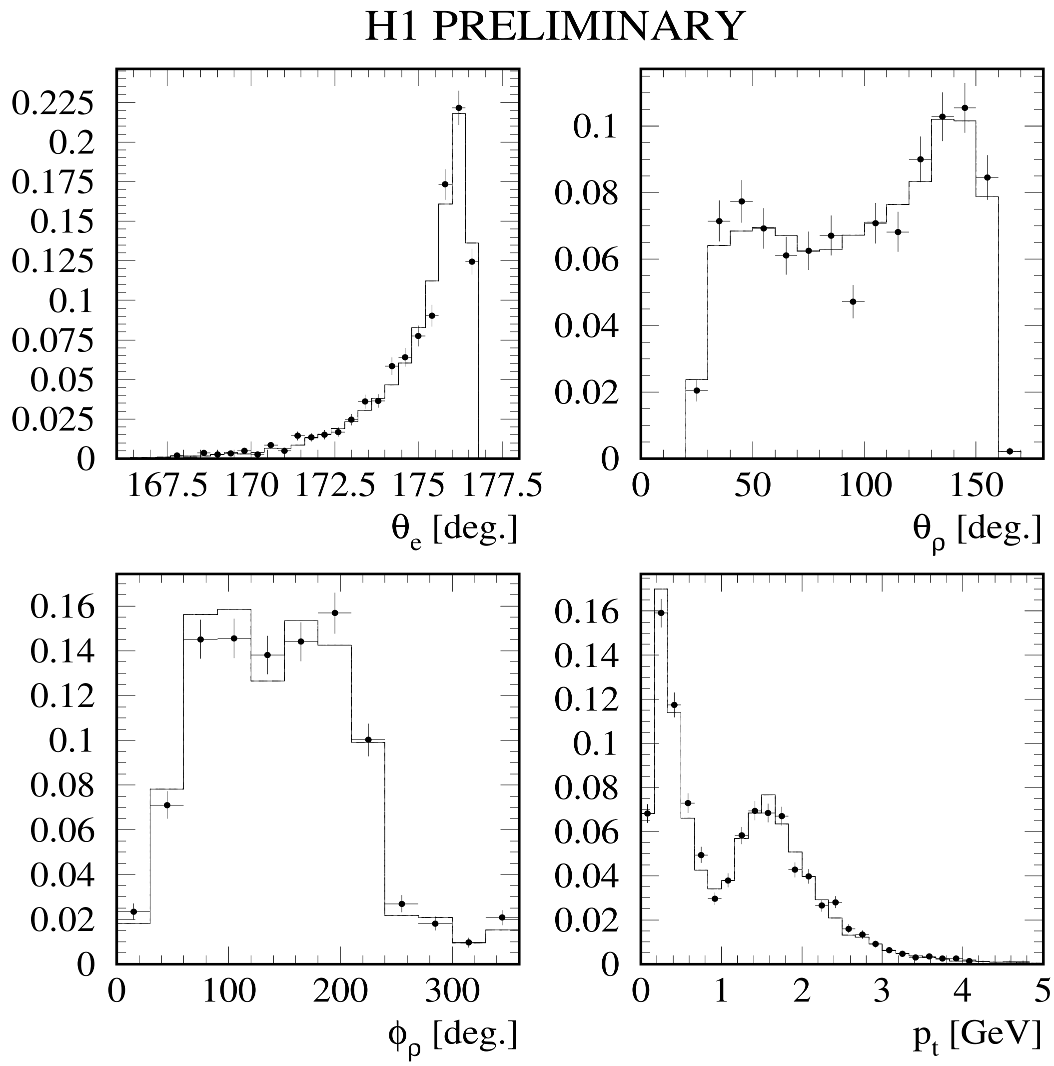

Figure 1: Uncorrected distributions of the polar angle of the scattered electron, the polar angle of the ρ meson, the azimuthal angle of the ρ meson, and the transverse momenta of the pion candidates, for the 1996 data sample (points) and for the Monte-Carlo simulation (histograms).

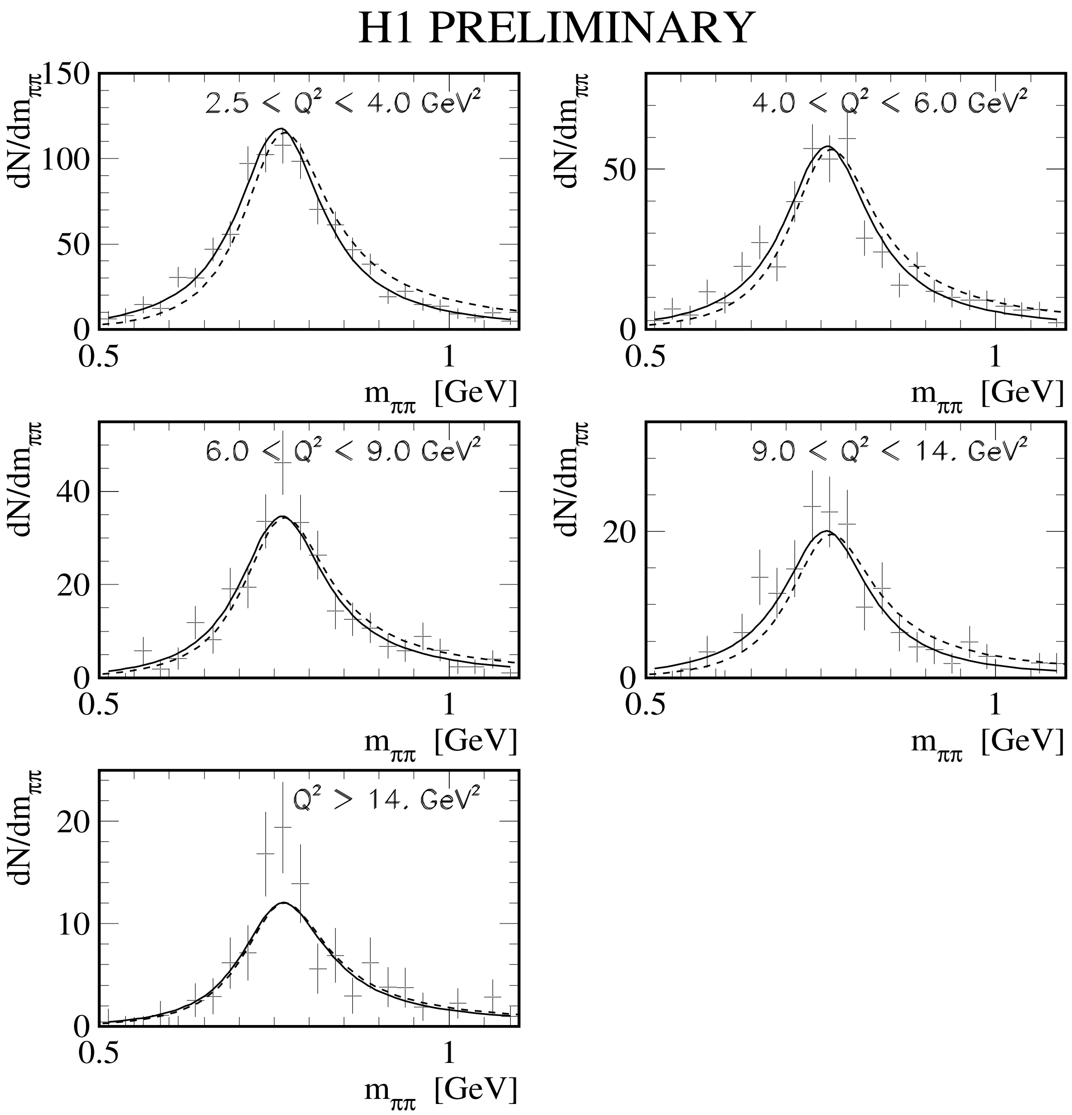

Figure 2: Acceptance corrected $m_{\pi\pi}$ mass distributions for the final 1996 data sample, after statistical substraction of the remaining ω and ϕ backgrounds, divided into five Q^2 bins. The superimposed curves are the result of fits to skewed relativistic Breit-Wigner distributions using the Ross-Stodolsky parameterisation of eq. 18, with the ρ mass and width fixed at the PDG values and assuming no non-resonant background. The solid lines are the result of the fits, the dashed lines correspond to the non-skewed Breit-Wigner contributions. The errors on the data are statistical only.

H1 PRELIMINARY

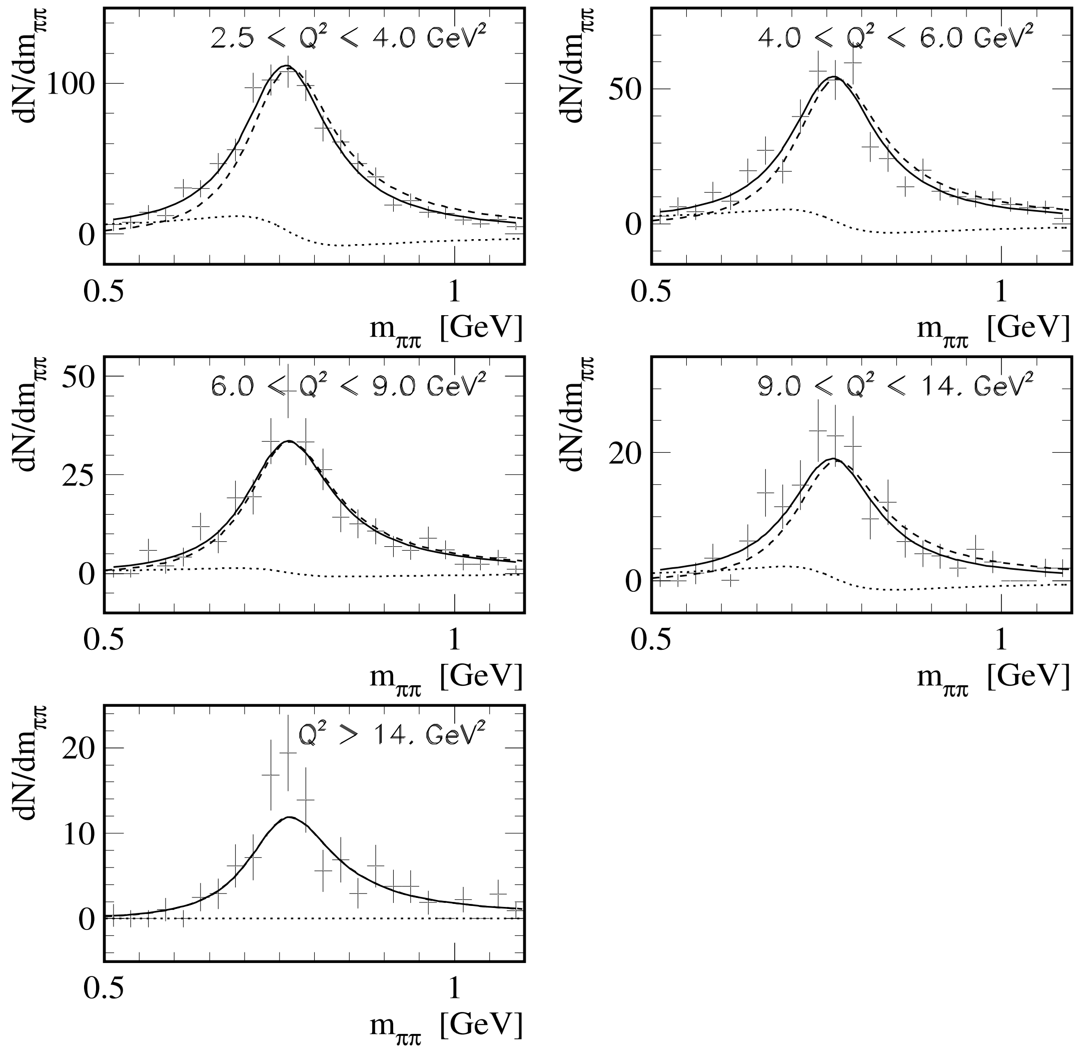

Figure 3: The data are the same as are shown in fig. 2 but are compared to the Söding parameterisation of eq. 22. The solid lines are the result of the fits, the dashed lines correspond to the non-skewed Breit-Wigner contributions, and the dotted lines correspond to the interferences between the resonant and the non–resonant amplitudes. The errors on the data are statistical only.

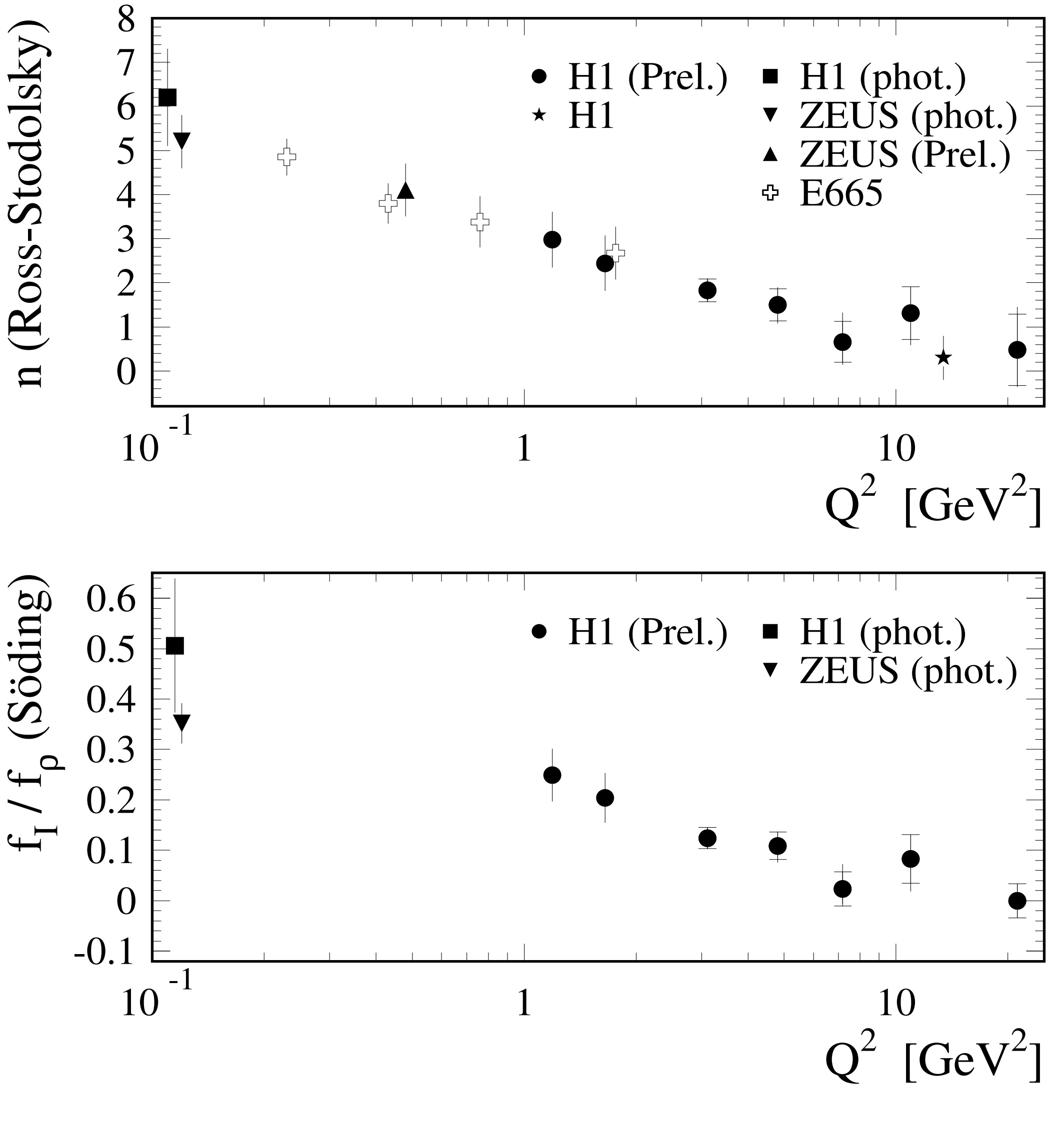

Figure 4: Q^2 dependence of the skewing parameters for elastic ρ production: n, for the Ross-Stodolsky parameterisation of eq. 18, and f_I/f_ρ, for the Söding parameterisation of eq. 22. The inner error bars are purely statistical, and the full error bars include the systematic errors added in quadrature. The data noted "phot." are for the photoproduction of ρ mesons ($Q^2 = 0$).

H1 PRELIMINARY

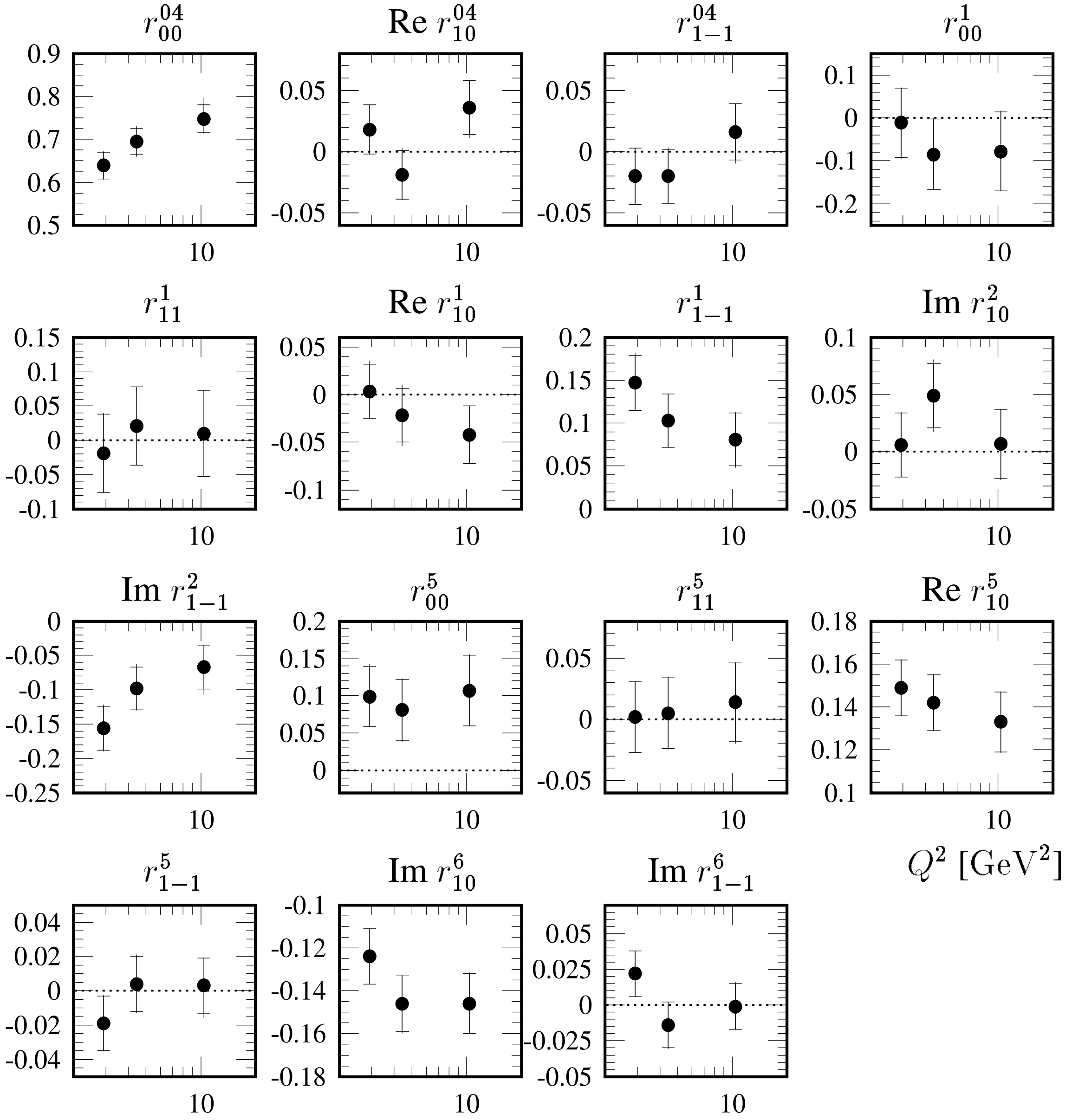

Figure 5: The full set of density matrix elements for elastic electroproduction of ρ mesons, for three values of Q^2. The inner error bars are purely statistical, and the full error bars include the systematic errors added in quadrature. The dashed lines indicate the expected null values in the case of natural parity exchange and s-channel helicity conservation.

H1 PRELIMINARY

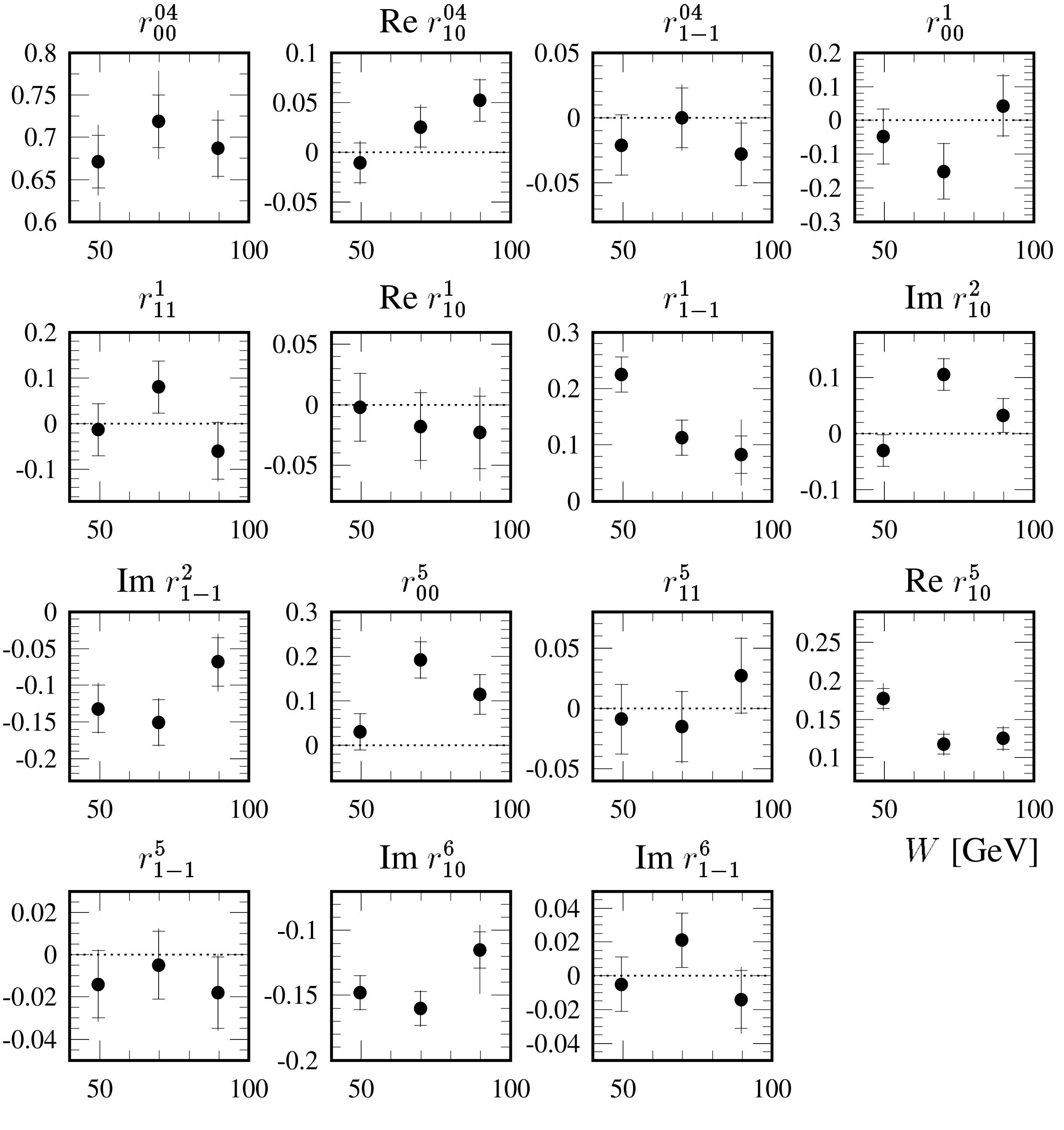

Figure 6: The full set of density matrix elements for elastic electroproduction of ρ mesons, for three values of W. The inner error bars are purely statistical, and the full error bars include the systematic errors added in quadrature. The dashed lines indicate the expected null values in the case of natural parity exchange and s-channel helicity conservation.

H1 PRELIMINARY

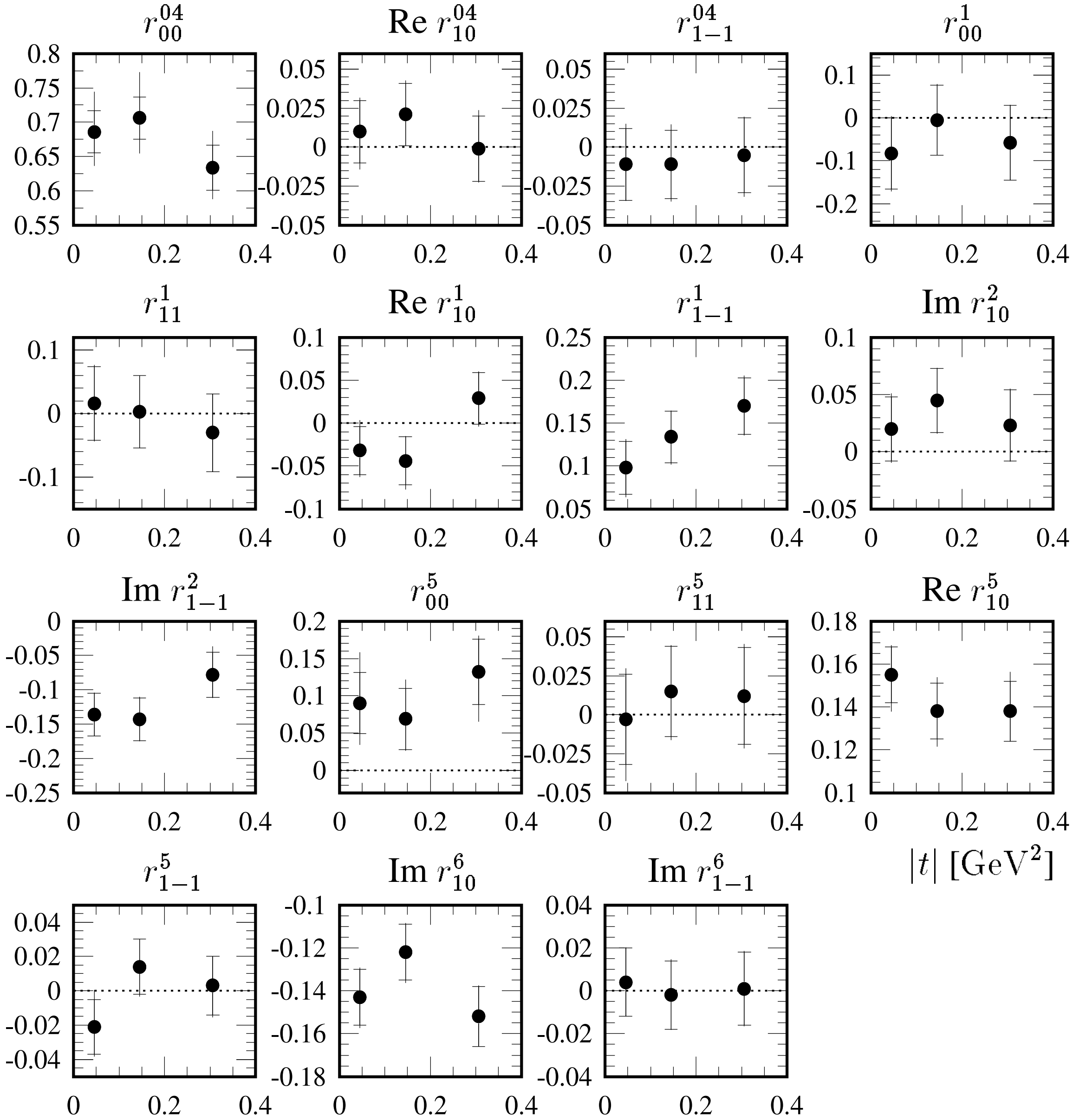

Figure 7: The full set of density matrix elements for elastic electroproduction of ρ mesons, for three values of t. The inner error bars are purely statistical, and the full error bars include the systematic errors added in quadrature. The dashed lines indicate the expected null values in the case of natural parity exchange and s-channel helicity conservation.

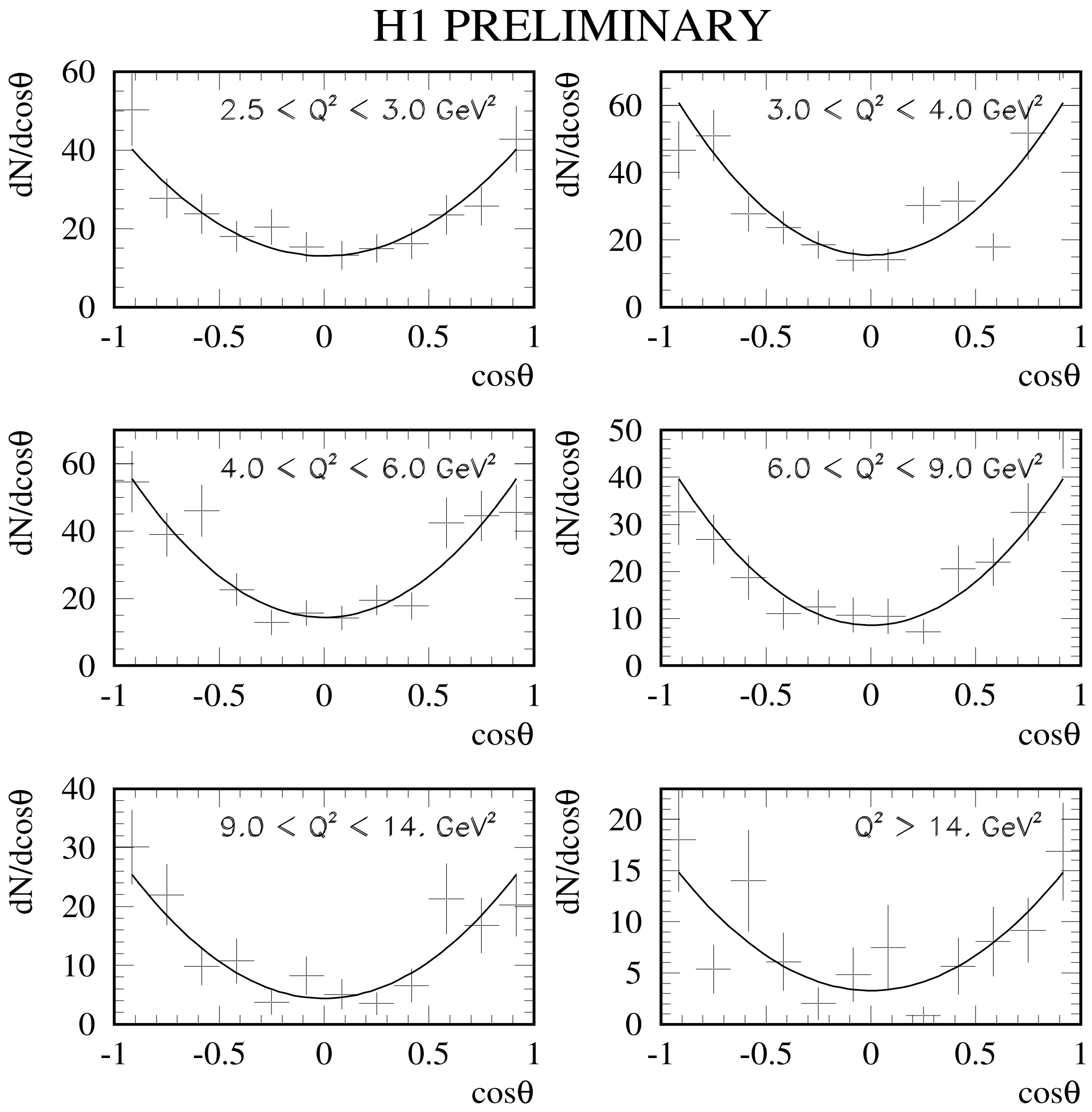

Figure 8: Acceptance corrected $\cos\theta$ distribution for the selected 1996 events in six bins in Q^2. The full curves are the result of fits of the form of eq. 30. The errors on the data points are statistical only.

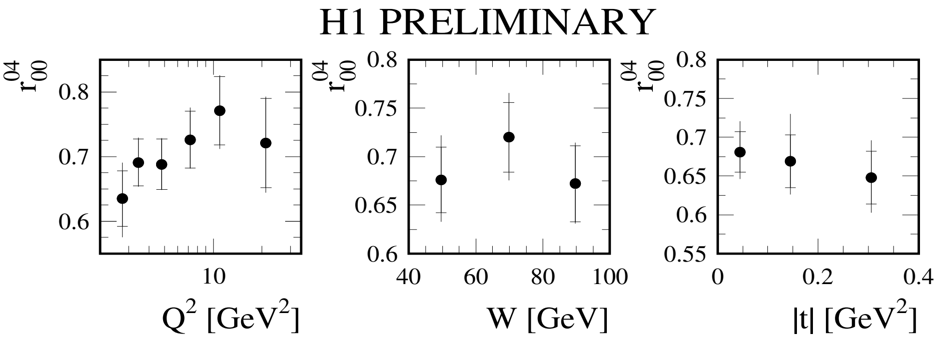

Figure 9: Measurements of the r_{00}^{04} matrix element as a function of Q^2, W and $|t|$, obtained from fits to the $\cos\theta$ distributions. The inner error bars are purely statistical and the full error bars include the systematic errors added in quadrature.

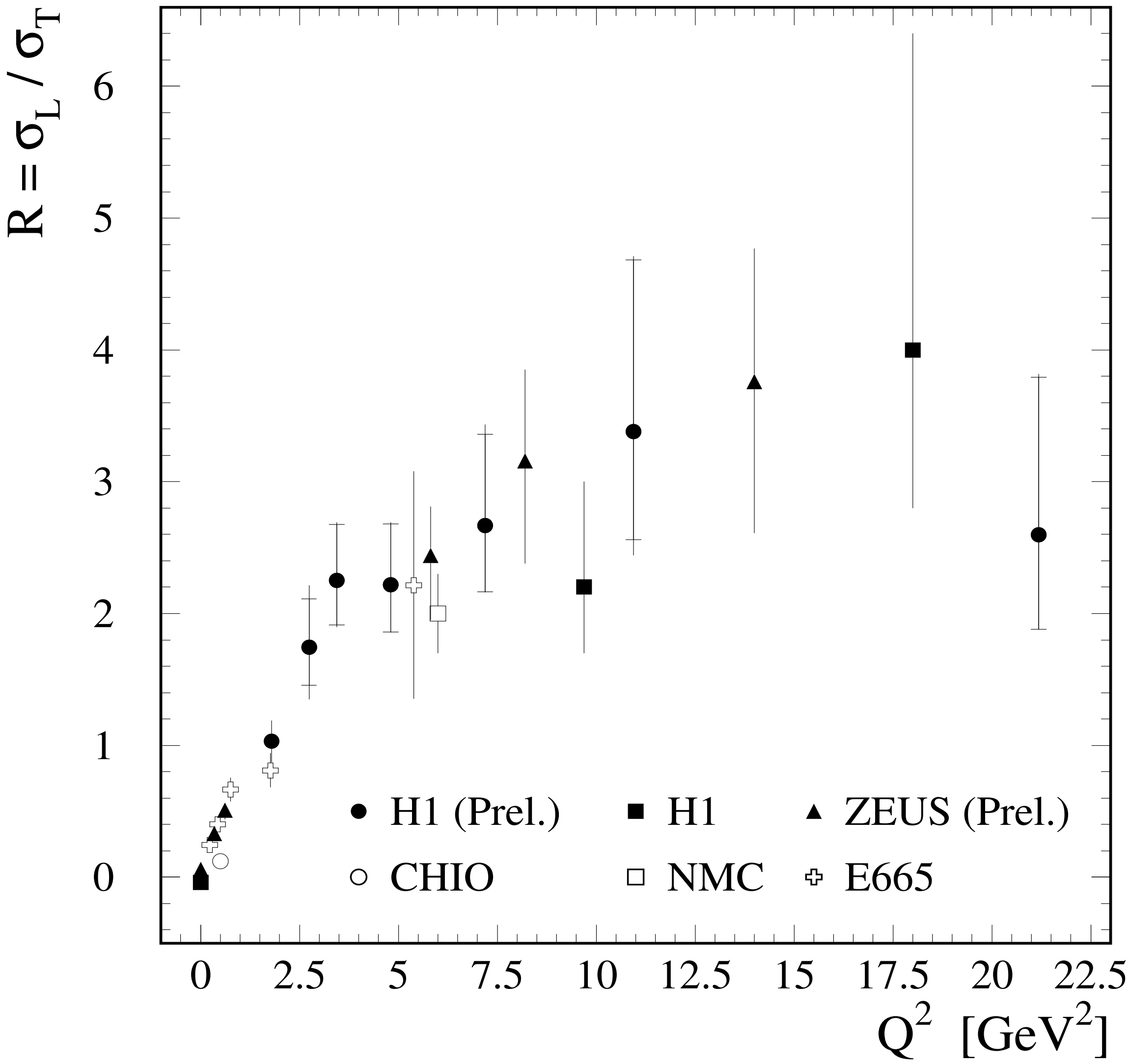

Figure 10: The ratio R of the longitudinal to transverse photon cross sections for elastic ρ meson electroproduction as a function of Q^2, for the present and other experiments, in the SCHC approximation. The inner error bars are purely statistical and the full error bars include the systematic errors added in quadrature.

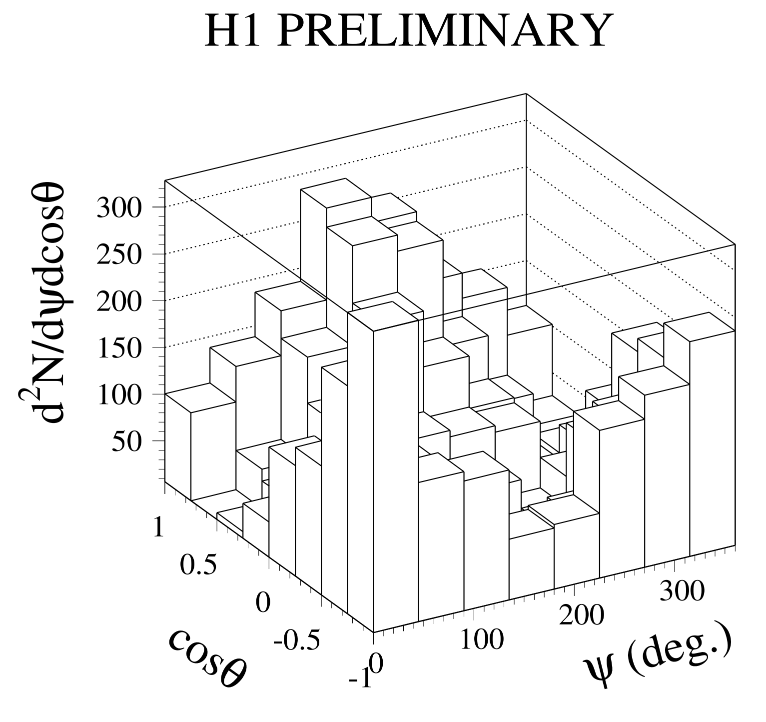

Figure 11: Acceptance corrected plot of the event distribution in the $\cos\theta$ and ψ angles for the 1996 data.

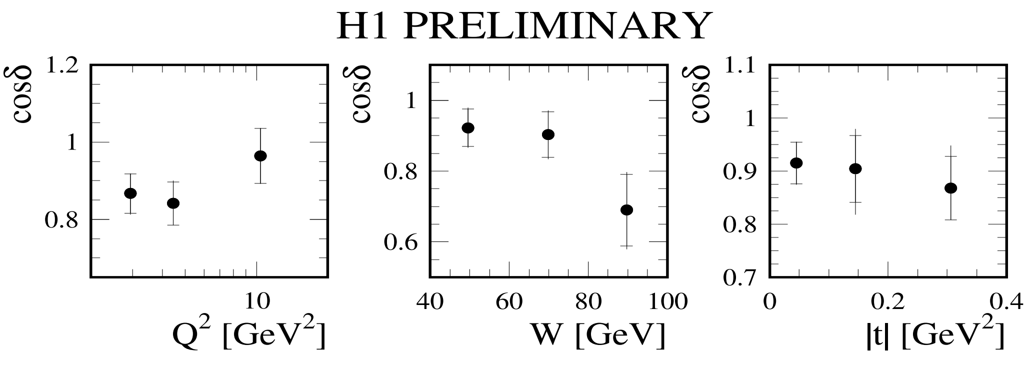

Figure 12: Measurements of the $\cos\delta$ parameter as a function of Q^2, W and t, obtained from fits to the $(\cos\theta, \psi)$ distributions. The inner error bars are purely statistical and the full error bars include the systematic errors added in quadrature.

H1 PRELIMINARY

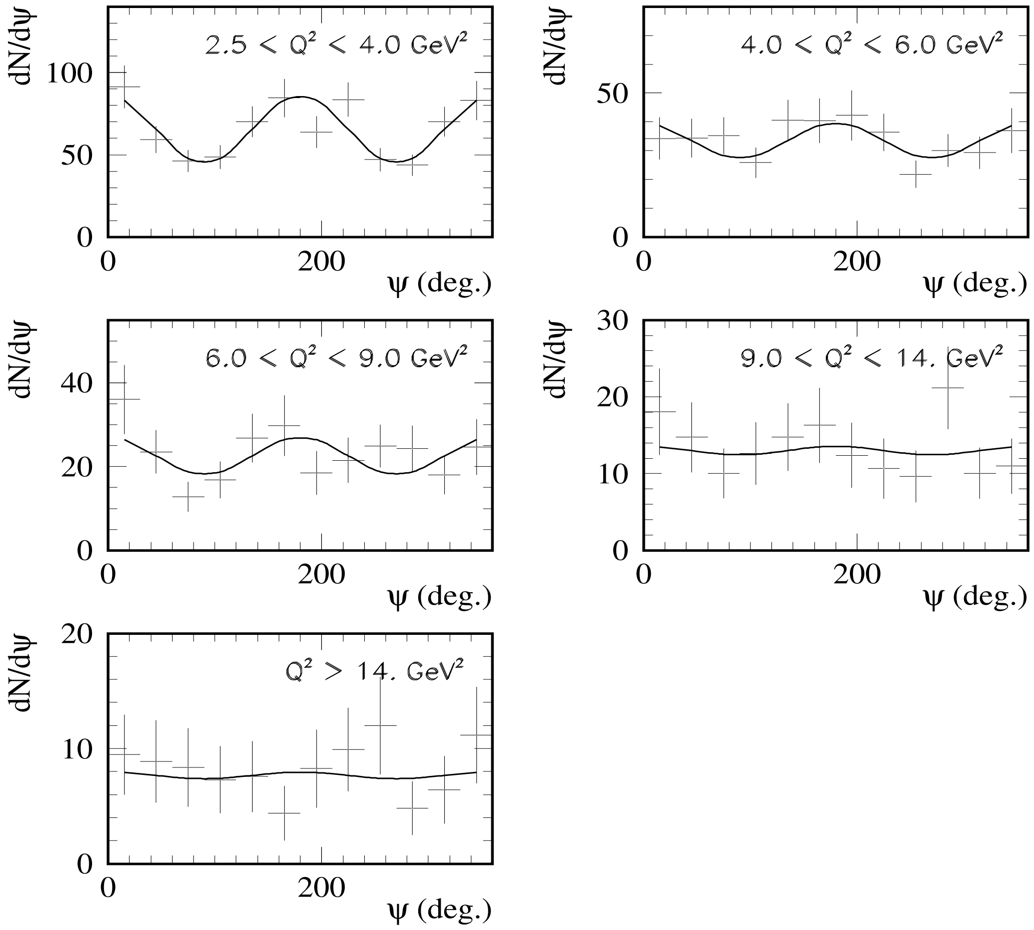

Figure 13: Acceptance corrected distribution of the ψ angle for the 1996 selected events in five bins in Q^2. The error bars are purely statistical.

H1 PRELIMINARY

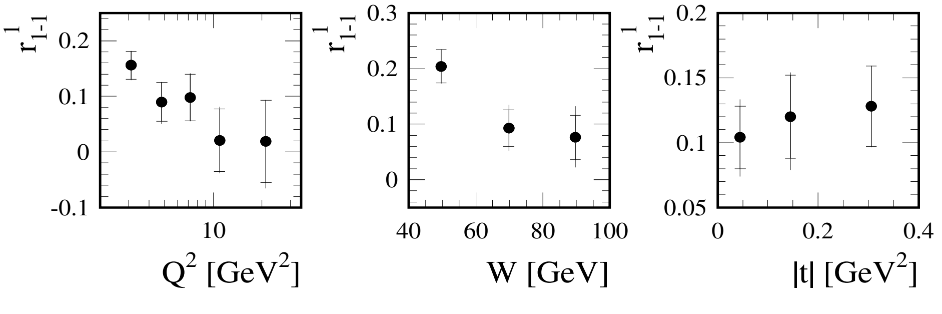

Figure 14: Measurements of the r^1_{1-1} matrix element in five bins in Q^2, three bins in W and three bins in t, under the SCHC approximation, obtained from fits to the ψ distributions. The inner error bars are purely statistical and the full error bars include the systematic errors added in quadrature.

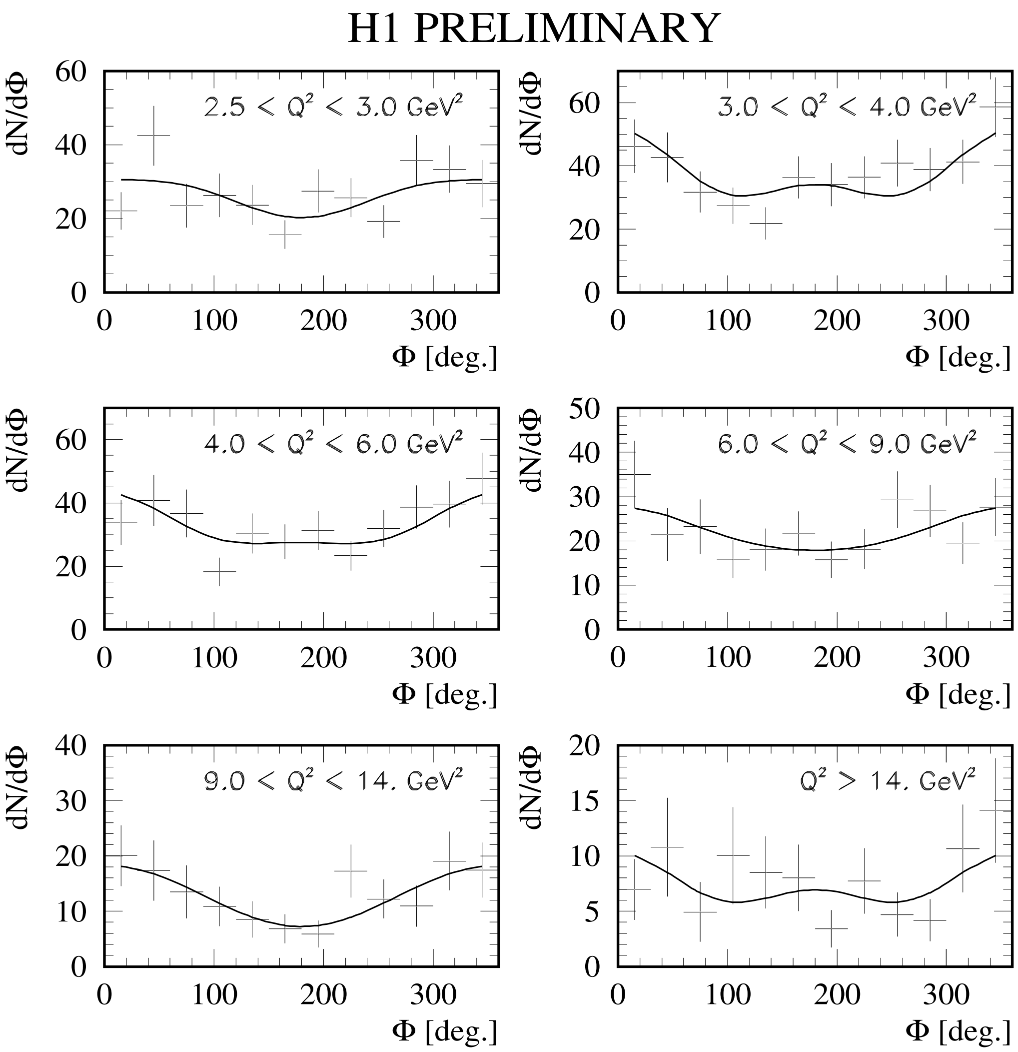

Figure 15: Acceptance corrected distribution of the ϕ angle for the 1996 selected events in six bins in Q^2. The errors on the data points are statistical only.

H1 PRELIMINARY

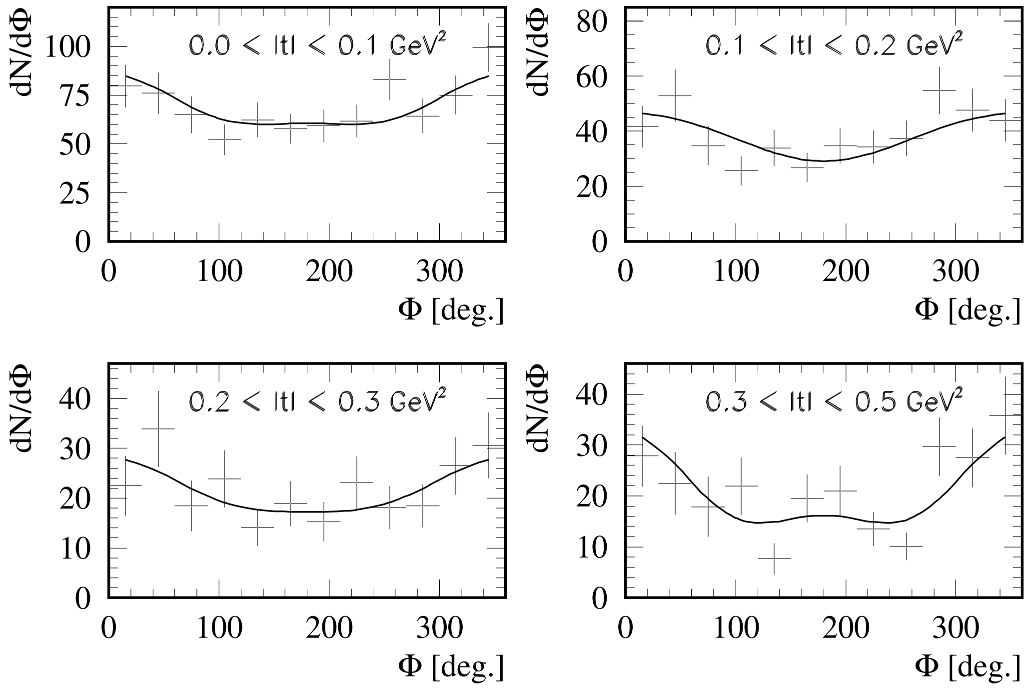

Figure 16: Acceptance corrected distribution of the ϕ angle for the 1996 selected events in four bins in t. The errors on the data points are statistical only.

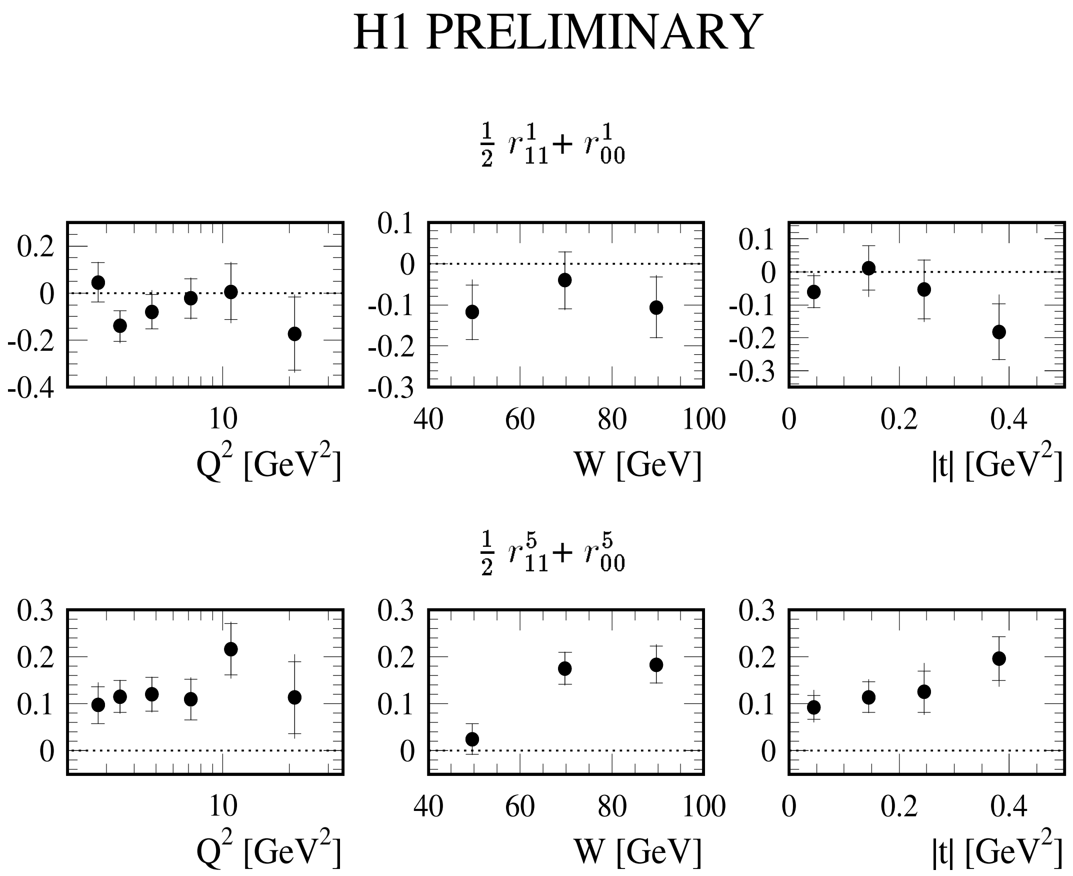

Figure 17: Measurements of the combinations of matrix elements $\frac{1}{2}r^1_{11}+r^1_{00}$ and $\frac{1}{2}r^5_{11}+r^5_{00}$, in six bins in Q^2, three bins in W and four bins in t, obtained from fits to the ϕ distributions. The inner error bars are purely statistical, and the full error bars include the systematic errors added in quadrature. The dashed lines indicate the expected null values in the case of natural parity exchange and s-channel helicity conservation.

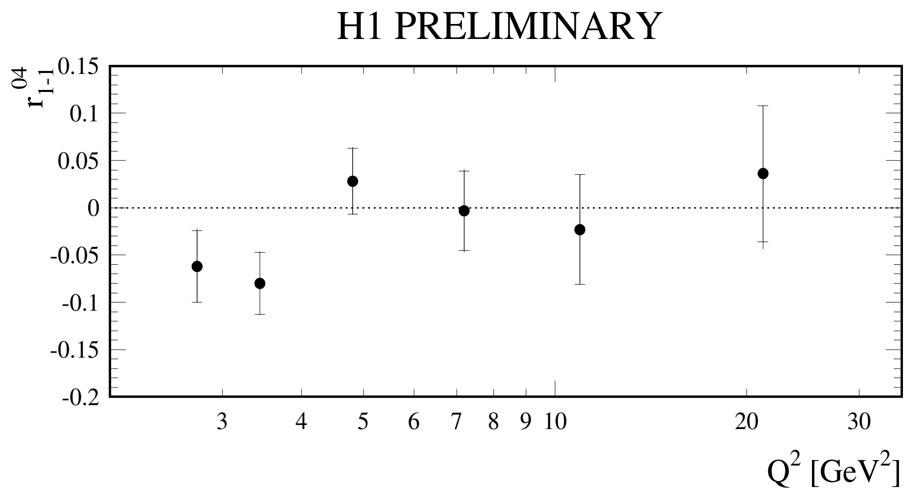

Figure 18: Measurements of the r^{04}_{1-1} matrix element as a function of Q^2, obtained from fits to the φ distributions. The inner error bars are purely statistical, and the full error bars include the systematic errors added in quadrature. The dashed lines indicate the expected null values in the case of natural parity exchange and s-channel helicity conservation.

H1 PRELIMINARY

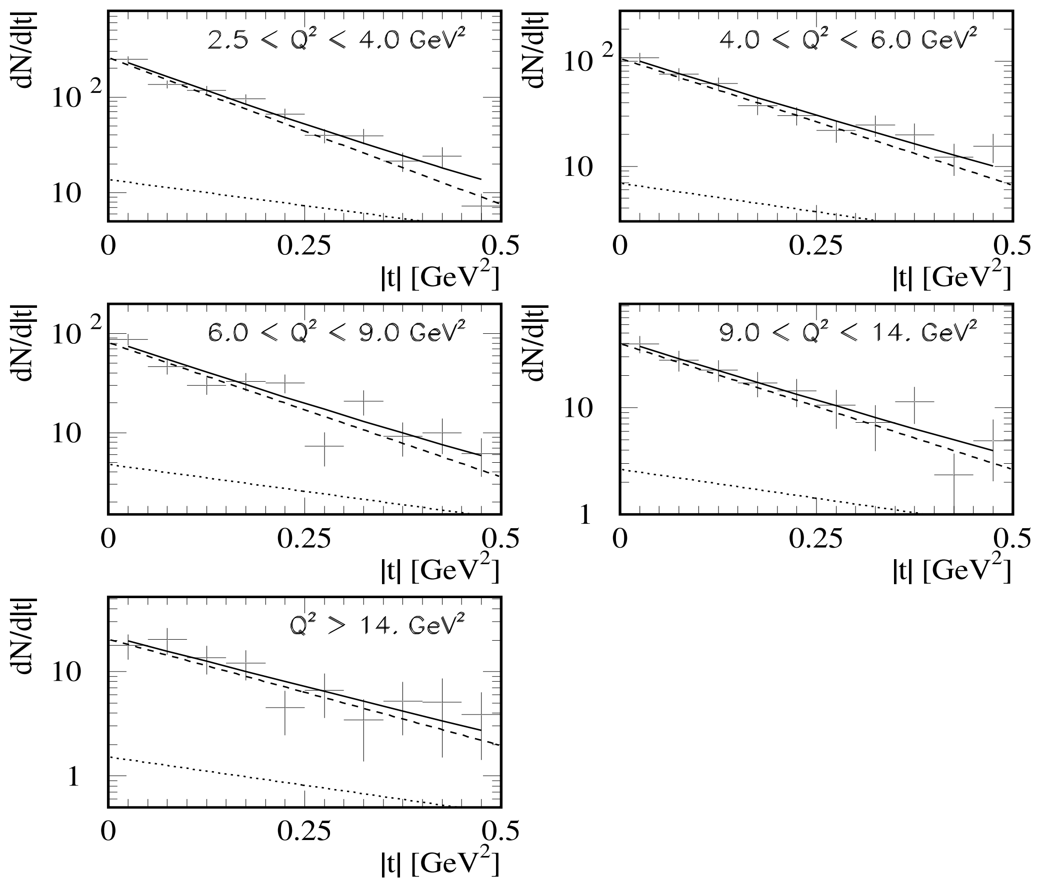

Figure 19: Acceptance corrected t distribution of the 1996 selected events for five bins in Q^2. The full lines correspond to a global fit of the distributions as the sum of three exponentials, describing respectively the elastic signal (dashed lines), the 11 % background of proton dissociation events with slope $b = 2.5$ GeV^{-2}(dotted line), and 1 % non-resonant background with slope of 0.3 GeV^{-2}. The errors on the data points are statistical only.

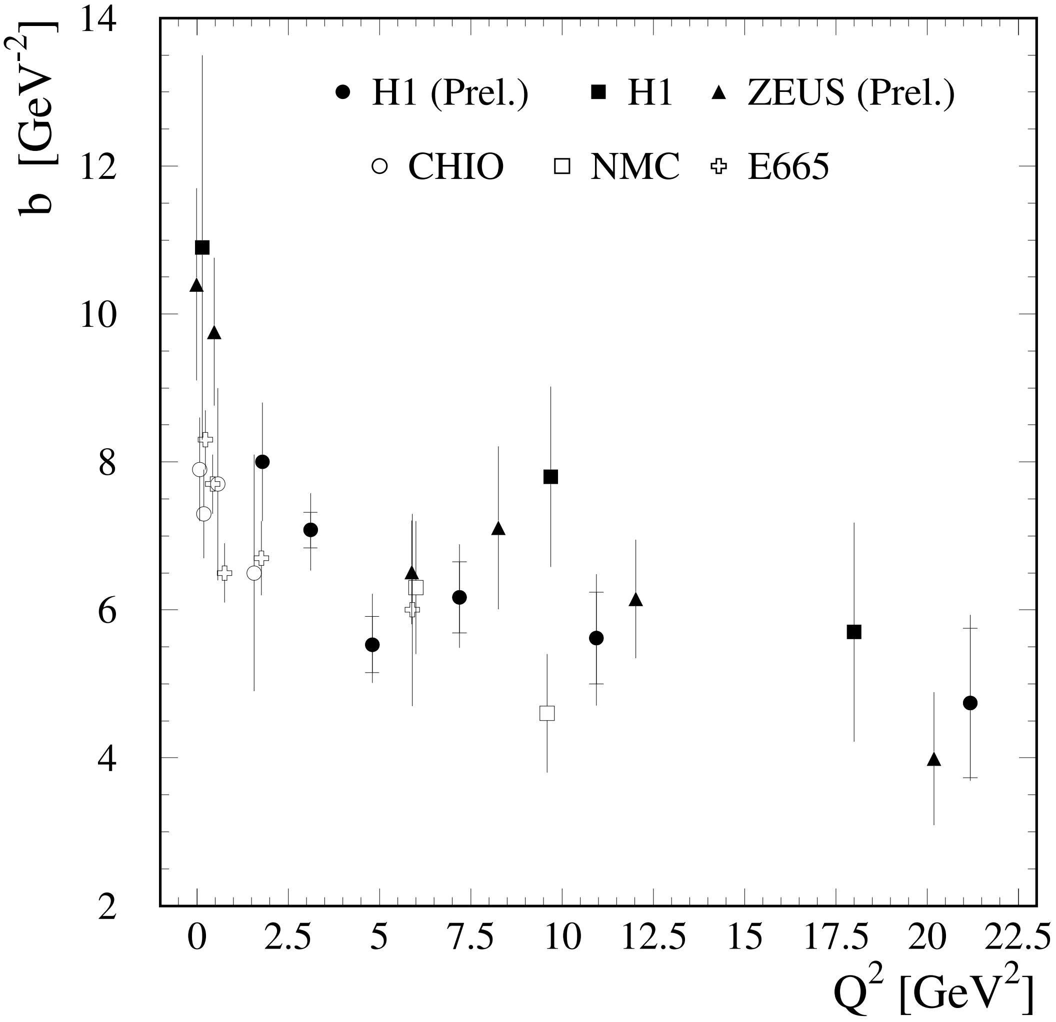

Figure 20: Q^2 dependence of the slope parameter b for elastic ρ production, for HERA and for fixed target experiments. The inner error bars are purely statistical, and the full error bars include the systematic errors added in quadrature.

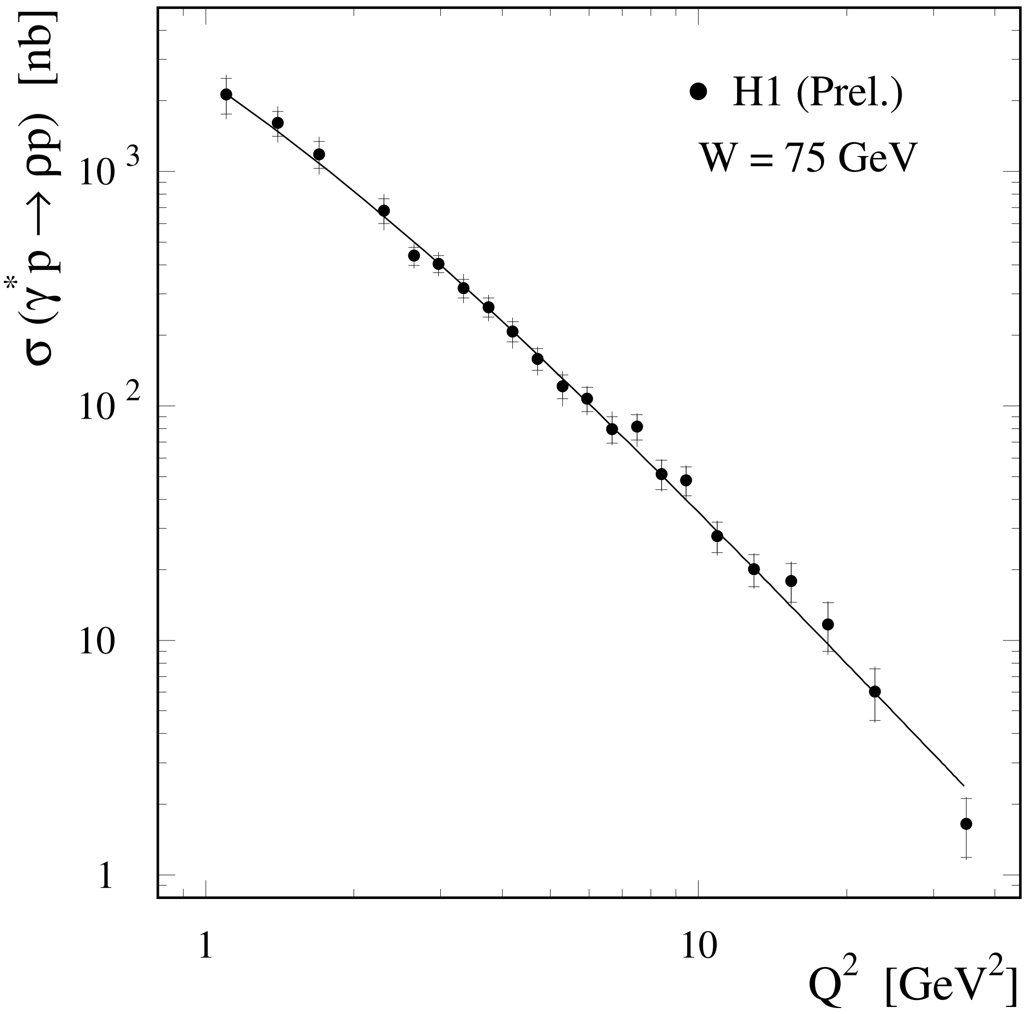

Figure 21: Cross section for the process $\gamma^* p \rightarrow \rho p$, as a function of Q^2, quoted for $W = 75$ GeV. The inner error bars are purely statistical, and the full error bars include the systematic errors added in quadrature. The curve corresponds to a fit of the form of eq. 47.

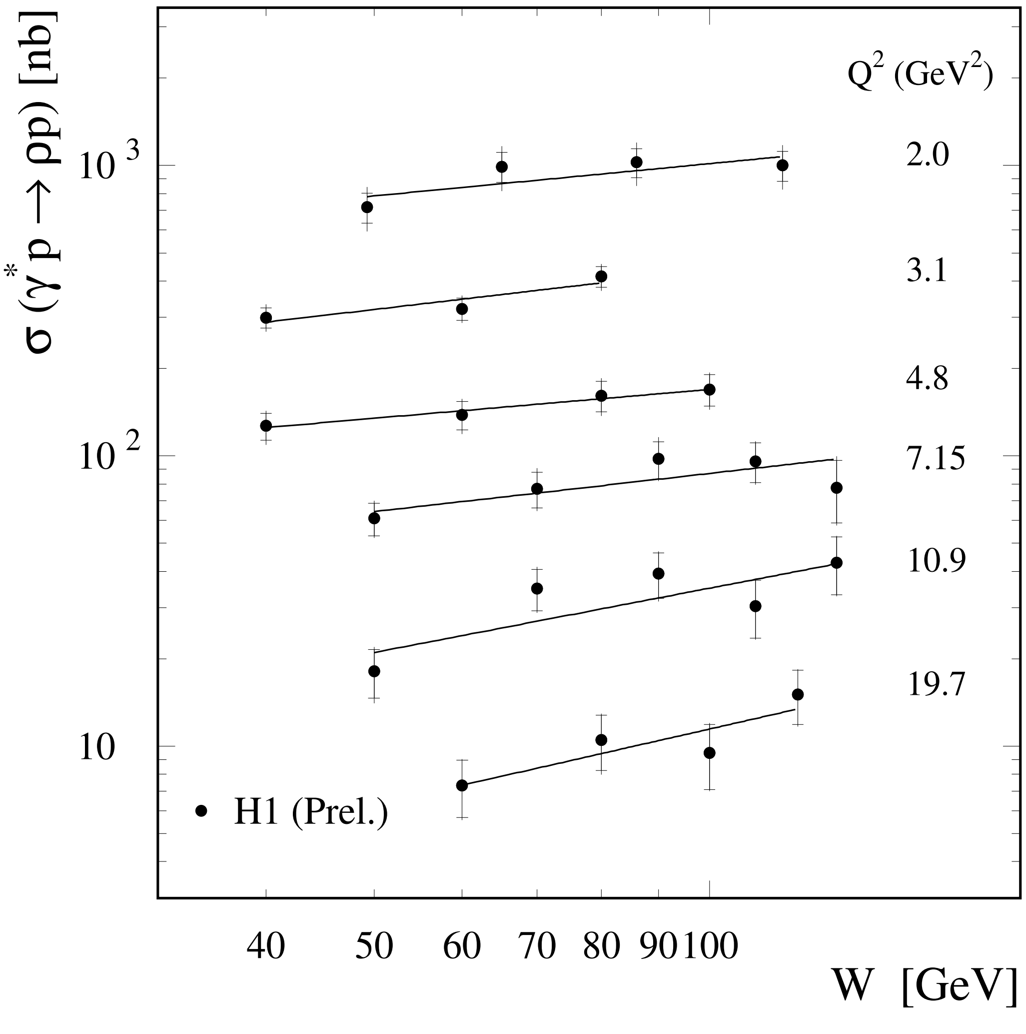

Figure 22: Cross section for the process $\gamma^* p \to \rho p$, as a function of W, for several values of Q^2. The inner error bars are purely statistical, and the full error bars include the systematic errors added in quadrature. The curves correspond to a fit of the form of eq. 49.

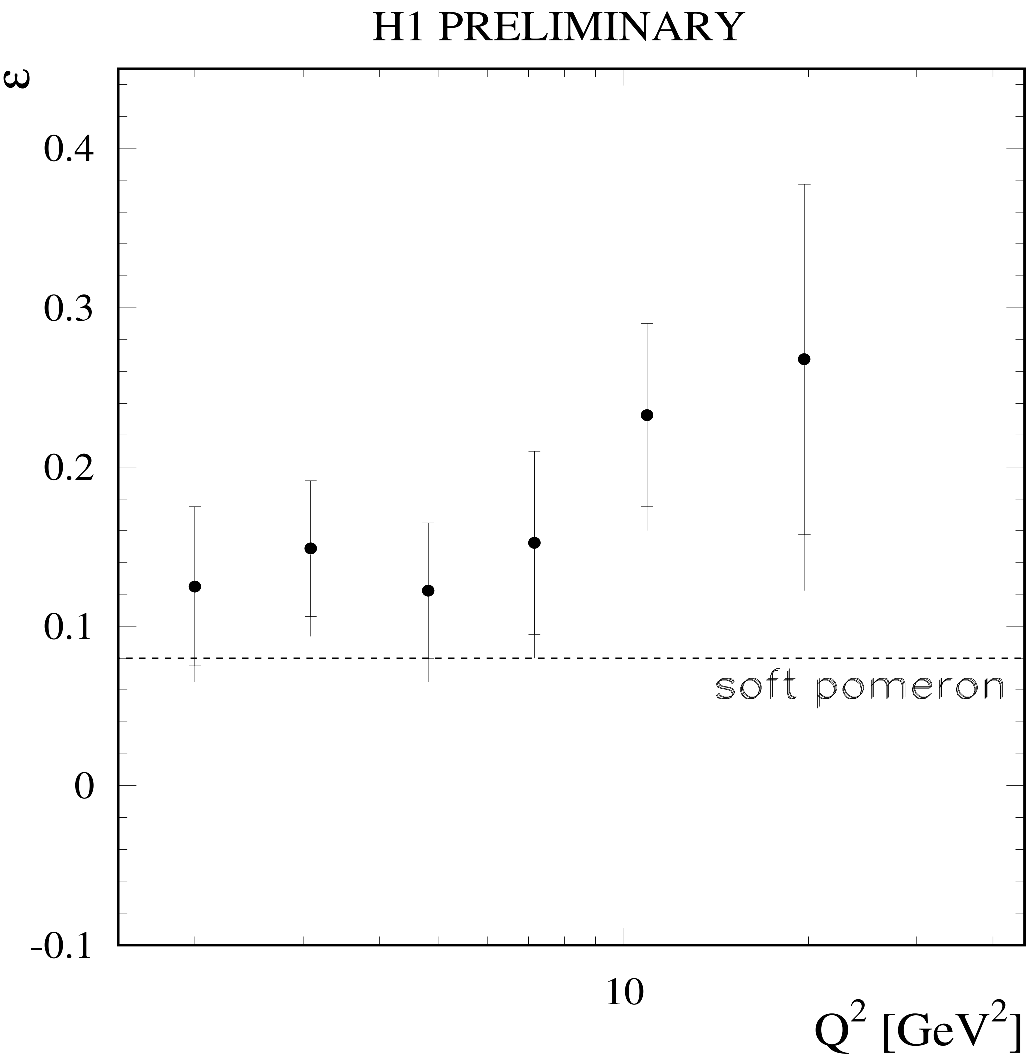

Figure 23: Q^2 dependence of the ϵ parameter (see eq. 49 and 51). The inner error bars come from the statistical and non-correlated systematic uncertainties on the cross section measurements, the outer error bars include the variation of the ϵ parameter when supposing $\alpha' = 0$, added in quadrature.